

1 **A coupled soilscape-landform evolution model: Model formulation**
2 **and initial results**

3

4

5

6

7 W. D. Dimuth P. Welivitiya^{1,2}, Garry R Willgoose¹, Greg R Hancock²

8 ¹School of Engineering, The University of Newcastle, Callaghan, 2308, Australia.

9 ²School of Environment and Life Sciences, The University of Newcastle, Callaghan, 2308,
10 Australia.

11 Corresponding Author: Garry Willgoose

12 Garry.willgoose@newcastle.edu.au

13

14

15

16

17

18

19

20

21

22 **Abstract**

23 This paper describes the coupling of the State Space Soil Production and Assessment Model
24 (SSSPAM) soilscape evolution model with a landform evolution model to integrate soil profile
25 dynamics and landform evolution. SSSPAM is a computationally efficient soil evolution model which
26 was formulated by generalising the mARM3D modelling framework to further explore the soil profile
27 self-organization in space and time, and its dynamic evolution. The landform evolution was integrated
28 into SSSPAM by incorporating the processes of deposition and elevation changes resulting from erosion
29 and deposition. The complexities of the physically based process equations were simplified by
30 introducing state-space matrix methodology that allows efficient simulation of mechanistically linked
31 landscape and pedogenesis processes for catena spatial scales. SSSPAM explicitly describes the particle
32 size grading of the entire soil profile at different soil depths, tracks the sediment grading of the flow,
33 and calculates the elevation difference caused by erosion and deposition at every point in the soilscape
34 at each time step. The landform evolution model allows the landform to change in response to (1)
35 erosion and deposition, and (2) spatial organisation of the co-evolving soils. This allows comprehensive
36 analysis of soil landform interactions and soil self-organization. SSSPAM simulates fluvial erosion,
37 armouring, physical weathering, and sediment deposition. The modular nature of the SSSPAM
38 framework allows integration of other pedogenesis processes to be easily incorporated. This paper
39 presents the initial results of soil profile evolution on a dynamic landform. These simulations were
40 carried out on a simple linear hillslope to understand the relationships between soil characteristics and
41 the geomorphic attributes (e.g. slope, area). Process interactions which lead to such relationships were
42 also identified. The influence of the depth dependent weathering function on soilscape and landform
43 evolution was also explored. These simulations show that the balance between erosion rate and
44 sediment load in the flow accounts for the variability in spatial soil characteristics while the depth
45 dependent weathering function has a major influence on soil formation and landform evolution. The
46 results demonstrate the ability of SSSPAM to explore hillslope and catchment scale soil and landscape
47 evolution in a coupled framework.

48

49

50

51

52

53

54 **1. Introduction**

55 Soil is one of the most important substances found on planet Earth. As the uppermost
56 layer of the earth surface, soil supports all the terrestrial organisms ranging from microbes to
57 plants to humans and provides the substrate for terrestrial life [*Lin, 2011*]. Soil provides a
58 transport and a storage medium for water and gases (e.g. carbon dioxide which influences the
59 global climate) [*Strahler and Strahler, 2006*]. The nature of the soil heavily influences both
60 geomorphological and hydrological processes [*Bryan, 2000*]. In addition to the importance of
61 soil from an environmental standpoint, it provides a basis for human civilization and played an
62 important role in its advancement through the means of agricultural development [*Jenny,*
63 *1941*]. Understanding the formation and the global distribution of soil (and its functional
64 properties) is imperative in the quest for sustainable use of this resource.

65 Characterization of soil properties at a global scale by sampling and analysis is time
66 consuming and prohibitively expensive due to the dynamic nature of the soil system and its
67 complexity [*Hillel, 1982*]. However over the years researchers have found strong links between
68 different soil properties and the geomorphology of the landform on which they reside [*Gessler*
69 *et al. 2000, 1995*]. Working on this relationship several statistical methods have been
70 developed to determine and map various soil properties depending on other soil properties and
71 geomorphology such as pedotransfer functions, geostatistical approaches, and state-factor (e.g.
72 clorpt) approaches [*Behrens and Scholten, 2006*]. Pedotransfer functions (PTFs) use easily
73 measurable soil attributes such as particle size distribution, amount of organic matter, and clay
74 content to predict hard to measure soil properties such as soil water content. Although very
75 useful, PTFs need a large database of spatially distributed soil property data and require site
76 specific calibration [*Benites et al., 2007*]. Geostatistical methods use a finite number of field
77 samples to interpolate the soil property distribution over a large area. Developing soil property
78 maps using geostatistical methods is possible for smaller spatial scales, however soil sampling
79 and mapping soil attributes can be prohibitively expensive and time consuming for larger
80 spatial domains [*Scull et al., 2003*]. State-factor methods, such as scorpan (developed by
81 introducing existing soil types and geographical position to clorpt framework) use digitized
82 existing soil maps and easily measurable soil attribute data to generate spatially distributed soil
83 property data using mathematical concepts such as fuzzy set theory, artificial neural network
84 or decision tree methods [*McBratney et al., 2003*]. However these techniques also suffer from
85 scalability issues and the typical need for site specific calibration.

86 While spatial mapping of soil properties is important, understanding the evolution of
87 these soil properties and processes responsible for observed spatial variability of soil properties
88 is also important. In order to quantify these processes and predict the soil characteristics
89 evolution through time, dynamic process based models are required [*Hoosbeek and Bryant,*
90 1992]. These mechanistic process models predict soil properties using both geomorphological
91 attributes and various physical processes such as weathering, erosion, and bioturbation
92 [*Minasny and McBratney, 1999*]. ARMOUR developed by *Sharmeen and Willgoose* [2006] is
93 one of the earliest process based pedogenesis models. ARMOUR simulated surface armouring
94 based on erosion and size selective entrainment of sediments driven by rainfall events and
95 overland flow, and physical weathering of the soil particles which break down the surface
96 armour layer. However, very high computational resource requirements and long run times
97 prevented ARMOUR from performing simulations beyond short hillslopes. Subsequently
98 *Cohen et al.* [2009] developed mARM by implementing a state-space matrix methodology to
99 simplify the process based equations and calibrated its process parameters using the results
100 from ARMOUR. Its high computational efficiency allowed mARM to explore soil evolution
101 characteristics on spatially distributed landforms. Through their simulations *Cohen et al.*
102 [2009] found a strong relationship between the geomorphic quantities contributing area, slope,
103 and soil surface grading d_{50} . Both ARMOUR and mARM simulate a surface armour layer and
104 a semi-infinite subsurface soil layer which supplies sediments to the upper armour layer. For
105 this reason both of these models were incapable of exploring the evolution of subsurface soil
106 profiles. To overcome this limitation *Cohen et al.* [2010] developed mARM3D by
107 incorporating multiple soil layers into mARM modelling framework. To generalise the work
108 of *Cohen et al.* [2010], [*Welivitiya et al., 2016*] developed a new soil grading evolution model
109 called SSSPAM, which was based on the approach of mARM3D and showed that the area-
110 slope- d_{50} relationship in *Cohen et al.* [2009] was robust against changes in process and climate
111 parameters and that the relationship is also true for all the subsurface soil layers, not just the
112 surface. Although these models predict the properties of the soil profile at an individual pixel,
113 they do not model the spatial interconnectivity between different parts of the soil catena
114 resulting from transport-limited erosion and deposition. Lateral material movement and
115 particle redistribution through deposition is very important in determining the soil
116 characteristics such as soil depth and soil texture [*Chittleborough, 1992; Minasny and*
117 *McBratney, 2006*]. In order to correctly predict spatially distributed soil attributes and
118 determine the changes in soil attributes with time, coupling soil profile evolution with landform
119 evolution is important.

120 The first attempt to integrate soilscape evolution with landform evolution was done by
121 *Minasny and McBratney* [1999; 2001]. They used a single layer to model the influence of soil
122 and weathering processes on landform evolution. In addition to *Minasny and McBratney* [1999;
123 2001] there are a number of conceptual frameworks found in literature for developing coupled
124 soil profile-landform evolution models [*Sommer et al.*, 2008; *Yoo and Mudd*, 2008]. MILESD
125 [*Vanwallegem et al.* [2013] is a model which can simulate soil profile evolution coupled with
126 landform evolution. MILESD is built upon the conceptual framework of landscape-scale
127 models for soil redistribution by *Minasny and McBratney* [1999; 2001] and pedon-scale soil
128 formation model developed by *Salvador-Blanes et al.* [2007]. In MILESD the soil profile is
129 divided into four layers containing the bottommost bedrock layer and 3 soil layers above it
130 representing the A, B, and C soil horizons. MILESD was used to model soil development over
131 60,000 years for a field site in Werrikimbe National Park, Australia [*Vanwallegem et al.*,
132 2013]. They matched trends observed in the field such as the spatial variation of soil thickness,
133 soil texture and organic carbon content. A limitation of MILESD is that it only uses three layers
134 to represent the soil profile. Recently the soil evolution module used in MILESD has been
135 modified to incorporate additional layers and has been combined with the landform evolution
136 model LAPSUS to develop a new coupled soilscape-landform evolution model, LORICA
137 [*Temme and Vanwallegem*, 2015]. They found similar results for soil-landform interaction and
138 evolution similar to MILESD simulation results.

139 Since only three layers were used in MILESD, the representation of the particle size
140 distribution down the soil profile was limited. Although LORICA incorporated additional soil
141 layers into the MILESD modelling framework, detailed exploration of soil profile evolution or
142 interactions between landform evolution and soil profile evolution has not yet been done with
143 this model. Importantly, particle size distribution of the soil can be used as a proxy for various
144 soil attributes such as the soil moisture content [*Arya and Paris*, 1981; *Schaap et al.*, 2001].
145 The main objective of this paper is to present a new soilscape evolution model capable of
146 predicting the particle size distribution of the entire soil profile by integrating a previously
147 developed soil grading evolution model in to a landscape evolution model.

148 Here we present the methodology for incorporating sediment transport, deposition and
149 elevation changes of the landform in to SSSPAM modelling framework to create a coupled
150 soilscape-landform evolution model. Detailed information regarding the development and
151 testing of SSSPAM soil grading evolution model is provided in previous papers by the authors
152 ([*Cohen et al.*, 2010; *Welivitiya et al.*, 2016]). The main focus of this paper is to incorporate

153 landform evolution into the SSSPAM framework. In addition to the model development we
154 also present the initial results of coupled soilscape-landform evolution exemplified on a linear
155 hillslope.

156 **2. Model development.**

157 The introduction of a landform into the SSSPAM framework is done using a digital
158 elevation model. The structure of the landform evolution model follows that for transport-
159 limited erosion [Willgoose *et al.*, 1991] but modified so as to facilitate its coupling with the
160 soilscape soil grading evolution model SSSPAM described in [Welivitiya *et al.*, 2016]. Here a
161 regular square grid digital elevation model was used and converted into a two dimensional
162 array which can be easily processed and analysed in the Python/Cython programming language.
163 Using the “steepest-slope” criterion [Tarboton, 1997] the flow direction and the slope value of
164 the each pixel was determined. Then using the created flow direction matrix, the contributing
165 area of each pixel was determined using the “D8” method [O’Callaghan and Mark, 1984] with
166 a recursive algorithm.

167 The soil profile evolution of each pixel is determined using the interactions between
168 the soil profile and the flowing water at the surface. Figure 1 shows these layers and their
169 potential interactions. This is similar to the schematic for the standalone soil grading evolution
170 model but is different in that the erosion/deposition at the surface is a result of the imbalance
171 between upslope and downslope sediment transport. The water layer acts as the medium in
172 which soil particle entrainment or deposition occurs depending on the transport capacity of the
173 water at that pixel. The water provides the lateral coupling across the landform, by the sediment
174 transport process. The soil profile is modelled as several layers to reflect the fact that the soil
175 grading changes with soil depth depending on the weathering characteristics of soil. Erosion
176 of soil and/or sediment deposition occurs at the surface soil layer (surface armour layer).

177 SSSPAM uses the state-space matrix approach to evolve the soil grading through the
178 soil profile. The state-space matrix methodology used for soilscape evolution is presented in
179 detail elsewhere [Cohen *et al.*, 2009; 2010; Welivitiya *et al.*, 2016] and will not be discussed in
180 detail here. Using this method a range of processes (e.g. erosion, weathering, deposition) can
181 be represented and applied so that the total change of soil layers and their properties can be
182 determined [Cohen *et al.*, 2009; 2010]. Once the erosion and deposition mass is determined,
183 elevation changes are calculated and the digital elevation model is modified accordingly. Once
184 the algorithm completes modifying the digital elevation model matrix, the calculation of flow

185 direction and contributing area is done and the process is repeated until a given number of
 186 iterations (evolution time) is reached.

187 **2.1 Characterizing erosion and deposition.**

188 As described in *Welivitiya et al.* [2016], the SSSPAM soil grading evolution model
 189 used a detachment-limited erosion model to calculate the amount of erosion. In order to
 190 simulate deposition and to differentiate between erosion and deposition, a transport-limited
 191 model is incorporated into the soil grading evolution model SSSPAM. Before calculating the
 192 erosion or deposition at a pixel (i.e. grid cell/node) we determine the transport capacity of the
 193 flow at that particular pixel. The transport capacity determines if the pixel is being subjected
 194 to erosion or deposition. The calculation of the transport capacity at each pixel is done
 195 according to the empirical equation presented by *Zhang et al.* [2011] which was determined by
 196 flume scale sediment detachment experiments. The transport capacity at a pixel (node) T_c (kg/s)
 197 is given by,

$$198 \quad T_c = \left(K_1 Q^{\delta_1} S^{\delta_2} d_{50a}^{\delta_3} \right) \omega \quad (1)$$

199 where Q is the discharge per unit width ($m^3/s/m$) at the pixel, S is the slope gradient (m/m) and
 200 d_{50a} is the median diameter of the sediment load in the flow (m), K_1 , δ_1 , δ_2 , δ_3 are constants
 201 determined empirically and ω is the flow width (m) at the pixel. Q is

$$202 \quad Q = \frac{rA_c}{\omega} \quad (2)$$

203 where r is runoff excess generation ($m^3/s/m^2$) and A_c is contributing area (m^2) of that pixel.
 204 Using their flume particle detachment experiments *Zhang et al.* [2011] determined that
 205 $K_1 = 2382.32$, $\delta_1 = 1.26$, $\delta_2 = 1.63$, and $\delta_3 = -0.34$ gave the best fit to their experimental results
 206 (with an R^2 value of 0.98). If $\underline{\psi}_{in}$ is the mass vector of the incoming sediment to the pixel, then
 207 $L_{in} = \sum(\psi_{in_1}, \psi_{in_2} \dots \dots \dots \psi_{in_n})$ is the total mass of incoming sediments to that pixel
 208 transported by water. Here $\underline{\psi}_{in}$ represents the cumulative outflow sediment mass vectors of
 209 upstream pixels ($\sum \underline{\psi}_{out}$) which drain into the pixel in question and is determined using the
 210 flow direction matrix mentioned earlier. Using this method, SSSPAM can model the total mass
 211 of the eroded sediment as well as the grading of the eroded material. Depending on the total
 212 incoming sediment load at the pixel, L_{in} , the transport capacity T_c of the flow and the potential
 213 total erosion mass E_p , the amount of actual erosion E_a (kg/s) or deposition D (kg/s) can be

214 determined according to Table 1. The scenario (A) and (B) (in Table 1) leads to erosion and
 215 armouring while scenario (C) leads to deposition.

216 **2.2 Erosion, armouring and soil profile restructuring**

217 The calculation of potential erosion E_p and armouring of the soil surface is done as in
 218 *Welivitiya et al.* [2016] and *Cohen et al.* [2009]. The actual erosion E_a is then determined by
 219 adjusting the potential erosion E_p according to scenarios A or B (Table 1). When calculating
 220 the actual erosion E_a we determine only the total mass of the erodible material (although it
 221 should be remembered that total erosion is a function of the transport capacity which is in turn
 222 a function of the grading d_{50}). The actual erosion mass vector \underline{G}_e is determined using the total
 223 soil surface mass grading vector \underline{G} and erosion transition matrix \mathbf{A} . The method utilized to
 224 generate this erosion transition matrix \mathbf{A} is identical to that described in detail in *Welivitiya et*
 225 *al.* [2016] and *Cohen et al.* [2009] and will not be discussed in detail here. Briefly, the
 226 methodology is a size selective entrainment of soil particles from the surface due to erosion
 227 leaving the surface armour layer enriched with coarser material. It is similar to the approach of
 228 *Parker and Klingeman* [1982] which *Willgoose and Sharmeen* [2006] showed was the best fit
 229 to their field data for their ARMOUR surface armouring model. The eroded material is added
 230 to the sediment load flowing into the pixel and can be given as the outflow sediment mass
 231 vector $\underline{\psi}_{out}$.

$$232 \quad \underline{\psi}_{out} = \underline{\psi}_{in} + \underline{G}_e \quad (3)$$

233 The actual depth of erosion Δh_E (m) is calculated using the equation,

$$235 \quad \Delta h_E = \frac{E_a}{R_x R_y \rho_s} \quad (4)$$

234

236 where R_x and R_y are the grid cell dimensions (m) in the two cardinal direction (pixel
 237 resolution), and ρ_s is the bulk density of the soil material (kg/m^3). Here we assume that the
 238 bulk density ρ_s remains constant regardless of the soil grading and over the simulation time of
 239 the simulation.

240 As described by the above equations, mass is removed from the surface armour layer
 241 into the water flowing above. In SSSPAM, mass conservation of the surface armour layer is

242 achieved by adding a portion of soil from the 1st subsurface layer to the surface armour layer
243 equal to the mass entrained into the water flow. It is important to note that the material
244 resupplied to the surface armour have the same soil grading as the subsurface layer. So both
245 small particles and large particles are resupplied to the armour layer. Most of the time the net
246 effect of this material resupply and the size selective erosion will be enrichment of larger
247 particles and armour strengthening. Depending on the depth dependent weathering function the
248 relative coarseness of the subsurface layers can be less compared to armour layer. But once the
249 armour layer is reconfigured with the added material from below and removal of small particles
250 through erosion, again the net effect is armour strengthening. More detailed description of this
251 process can be found in *Cohen et al.* [2009] and *Welivitiya et al.* [2016]

252 This material resupply propagates down the soil profile (one soil layer supplying
253 material to the layer above and receiving material from the layer below) all the way to the
254 bedrock layer which is semi-infinite in thickness. Since the soil grading of different layers are
255 different to each other, this flux of material through the soil profile changes the soil grading of
256 all the subsurface layers. Conceptually the position of the modelled soil column moves
257 downward since all vertical distances for the soil layers are relative to the soil surface. In the
258 case of deposition the model space would move upwards (discussed in detail later). This
259 movement of the “soil model-space” during erosion is illustrated in Figure 2.

260 Note that erosion is limited by the imbalance between sediment transport capacity and
261 the amount of the sediment load in the flow as well as the threshold diameter of the particle
262 which can be entrained (Shield shear threshold, see *Cohen et al.* [2009] for details) by the water
263 flow. These factors limit the potential erosion rate at a pixel. During the test simulations
264 presented later in this paper, the depth of erosion Δh_E was always less than the surface armour
265 layer thickness D_{sur} (Figure 2(a)) and the rearrangement of the soil grading of all the layers
266 were straightforward.

267 **2.3 Sediment deposition**

268 If the total mass of incoming sediment L_{in} is higher than the transport capacity of the
269 sediment transport capacity T_c at the pixel (Table 1, Scenario C) deposition of sediments occurs
270 at the pixel. The mass of deposited material is the difference between L_{in} and T_c . Although
271 calculating the total mass of sediment which needs to deposit at a pixel (D) is straightforward,
272 determining the distribution of the deposited sediments in the form of deposition mass vector
273 $\underline{\Phi}$ is somewhat complicated. The deposition mass vector $\underline{\Phi}$ depends on the size distribution of

274 the incoming sediments which in turn depend on the erosion characteristics of the upstream
 275 pixels. The calculation of the deposition mass vector $\underline{\Phi}$ is done using the deposition transition
 276 matrix \mathbf{J} . Here $\underline{\Phi}$ is defined as,

$$278 \quad \underline{\Phi} = \frac{\underline{\psi}_{in} \mathbf{J}}{\sum J_{z,z} \psi_z} D + \underline{K} \quad (5)$$

277

279 where $J_{z,z}$ are the diagonal entries of \mathbf{J} (here and after the subscript z denotes the z^{th} grading
 280 class), and ψ_z are the elements of $\underline{\psi}_{in}$. \underline{K} is an adjustment vector which modifies the values in
 281 deposition mass vector $\underline{\Phi}$ such that $\Phi_z \leq \psi_z$, where Φ_z being the elements of the vector $\underline{\Phi}$.
 282 The adjustment vector \underline{K} ensures that deposited material from each size class is not greater than
 283 the total amount of sediment load available in the incoming sediment flow and is iteratively
 284 determined within the deposition module of SSSAPM. The following simplified example
 285 shows the need to have this adjustment vector and the method we used to calculate it.

286 Consider the example values given in Table 2. The total mass of the incoming sediments
 287 is 75 kg and the sediments are distributed in four size classes. Here the size class one is the
 288 largest and has the highest potential for deposition (with $J_{1,1} = 1$) while the size class four has
 289 the lowest potential for deposition (with $J_{4,4} = 0.1$). If the transport capacity T_c is 40 kg, 35 kg
 290 of incoming sediments should deposit at the pixel as the total deposition D . Using the $\sum J_{z,z} \psi_z$
 291 value (which is 24) and rescaling these values with D (total deposition mass), we can calculate
 292 the masses of sediment which need to be deposited from each grading class. In some cases
 293 (when the total deposition D is higher than the $\sum J_{z,z} \psi_z$ value) the mass of material which
 294 needs to be deposited can be larger than the available sediments in that particular size class. In
 295 this example there is 5 kg of sediments in the 1st size class and 10 kg of sediments in the second
 296 size class respectively. However, our adjusted calculation dictate that there should be 7.29 kg
 297 deposition from the 1st size class and 10.21 kg from the 2nd size class which is not possible.
 298 So these values needs to be adjusted to reflect maximum possible deposition from size classes
 299 one and two which are 5 kg and 10 kg respectively. This adjustment introduces a deficit of 2.5
 300 kg to the total deposition and it needs to be deposited from the 3rd and 4th smaller grading
 301 classes. According to the deposition matrix values $J_{z,z}$ the deposition probability ratio
 302 between 3rd and 4th grading class is 4:1 (0.4:0.1). The deficit mass 2.5kg is deposited from the
 303 3rd and 4th size class with 4:1 ratio which accounts to an additional deposition mass of 2 kg

304 from 3rd size class and 0.5 kg from the 4th size class. In this way the entries of the adjustment
305 vector \underline{K} are calculated. Depending on the number of size classes and the distribution of the
306 sediments, this adjustment vector \underline{K} needs to be calculated iteratively.

307 The deposition of material from the incoming sediment flow reduces the total mass of
308 the sediment load in the flow and changes its distribution due to this size selective deposition
309 (particles with higher settling velocity deposit faster). The outflow sediment mass vector $\underline{\psi}_{out}$
310 is then calculated by,

$$311 \quad \underline{\psi}_{out} = \underline{\psi}_{in} - \underline{\Phi} \quad (6)$$

312 Also the deposition height Δh_D is calculated using,

$$313 \quad \Delta h_D = \frac{D}{R_x R_y \rho_s} \quad (7)$$

314

315 The deposition height Δh_D can exceed the surface armour layer thickness (and even the
316 thickness of several soil layers, illustrated in Figure 2(b2), (c2), if the timestep is large) and the
317 restructuring of the soil layer grading can be complicated. One solution to this problem is to
318 use a smaller timestep. But we preferred to use a conceptualization that does not impact as
319 much on the numerical efficiency. Details on restructuring the soil column under deposition
320 are given in the following section.

321 The following section describes the methodology for deriving the deposition transition
322 matrix.

323 **2.3.1 Derivation of deposition transition matrix**

324 The deposition transition matrix is derived by considering the particle trajectories at the
325 pixel level. Assuming all the sediments flowing into the pixel are homogeneously distributed
326 throughout the water column, we define the critical immersion depth $h_{ct(z)}$ for all the particle
327 size classes as illustrated with Figure 3. The critical immersion depth is the vertical distance
328 travelled by the particle at the average settling velocity of the particle size class V_z where it will
329 travel the horizontal distance of the pixel width X under the flow with the fluid flow velocity
330 V_f and settle at the far edge (i.e. exit) of the pixel.

331
$$h_{ct(z)} = \frac{X}{V_f} V_z \quad (8)$$

332 Depending on the position of the sediment particle entering into the pixel with respect
 333 to critical immersion depth, whether or not that particle will deposit in that pixel can be
 334 determined. Particles entering to the pixel below the critical immersion depth will settle within
 335 the current pixel, while particles entering above the critical immersion depth will stay in
 336 suspension and exit the current pixel. The critical immersion depth is greater for larger (or
 337 denser) particles and less for smaller (or less dense) particles. For sediment particles in larger
 338 size classes, the critical immersion depth can be larger than the flow depth H_f (m) (thickness
 339 of the water column). That means all the particles in that particle size class will settle in the
 340 pixel. Using the critical immersion depth and the flow depth we can define the diagonal
 341 elements $J_{z,z}$ of the deposition transition matrix **J** in following manner.

342
$$J_{z,z} = \begin{cases} \frac{h_{ct(z)}}{H_f} & \text{for } H_f \geq h_{ct(z)} \\ 1 & \text{for } H_f < h_{ct(z)} \end{cases} \quad (9)$$

343 Note the deposition transition matrix **J** is a diagonal matrix which contains only
 344 diagonal elements (all off diagonal elements being 0). The evaluation of elements in the
 345 potential deposition matrix **J** requires the calculation of the critical immersion depth $h_{ct(z)}$ and
 346 the flow depth H_f .

347 The following discussion briefly describes the methodology used to calculate the above
 348 variables. The average settling velocity of all the particle sizes classes can be calculated for
 349 typical sediment sizes using Stoke's Law [*Lerman, 1979*].

351
$$V_z = \frac{(\rho_s - \rho_f)g}{18\mu} d_z^2 \quad (10)$$

350

352 where ρ_s and ρ_f are bulk density of the soil particles and the density of water (kg/m^3) (fluid),
 353 g is gravitational acceleration (m/s^2), d_z is the median particle diameter of the size class z (m)
 354 and μ is the dynamic viscosity of water (kg/s/m^2). The average flow velocity and the flow depth
 355 can be calculated using the Manning formula [*Meyer-Peter and Müller, 1948; Rickenmann,*
 356 *1994*]. Although the Manning formula is normally used to calculate the average flow velocity

357 in channels, we assume that the same formula can be used to calculate the flow velocity at the
 358 pixel level assuming water flowing over a pixel as a small channel segment. Manning formula
 359 states,

$$360 \quad V_f = \frac{1}{n} R^{2/3} S^{1/2} \quad (11)$$

361 where n is the Manning's roughness coefficient, R is the hydraulic radius (m) and S is the slope
 362 (m/m). The Manning's roughness coefficient n can be approximated using the median diameter
 363 d_{50} (mm) of the surface armour layer [Coon, 1998] using following equation.

$$364 \quad n = 0.034(d_{50})^{1/6} \quad (12)$$

365 The hydraulic radius is the ratio between the cross-sectional area of the flow and the
 366 wetted perimeter. When we consider the flowing water column at a pixel, the cross-sectional
 367 area of the flow is the multiplication of flow width (pixel width) ω and the flow depth H_f with
 368 the wetted parameter being the flow width ω . The hydraulic radius at the pixel is then the flow
 369 depth H_f . Substituting flow depth for hydraulic radius equation (11) becomes,

$$371 \quad V_f = \frac{1}{n} H_f^{2/3} S^{1/2} \quad (13)$$

370

372 The flow velocity at the pixel can be also expressed in terms of upslope contributing
 373 area A_c , runoff excess generation r , flow width ω and flow depth H_f .

$$374 \quad V_f = \frac{A_c r}{H_f \omega} \quad (14)$$

375 Solving the equations (13) and (14) the flow depth H_f and the flow velocity V_f can be
 376 calculated in terms of A_c , r , ω , S and n using

$$377 \quad H_f = \left(\frac{A_c r n}{\omega S^{1/2}} \right)^{3/5} \quad (15)$$

$$378 \quad V_f = \left(\frac{A_c r}{\omega} \right)^{2/5} \left(\frac{S^{3/2}}{n^3} \right)^{1/5} \quad (16)$$

379 2.3.2 Restructuring of the soil layers after deposition

380 Deposition of sediment on the soil surface moves the soil surface upwards (soil model-
381 space moves upwards). As mentioned earlier the deposition height Δh_D can exceed the surface
382 armour layer thickness and/or a number of subsurface soil layer thicknesses. Figure 2(b2)
383 illustrates a typical scenario where the deposition height has exceeded the thickness of the
384 surface armour layer D_{sur} .

385 Figure 2(b2) and (c2) shows the movement of the model-space for three soil layers. In
386 the restructured soil column (Figure 2(c2)) the new 3rd layer consists of a portion of the original
387 layer one (surface armour layer) and the 1st original subsurface layer. Because of the upward
388 movement of the model-space, a portion of the 2nd original soil layer and the entire 3rd soil layer
389 has been incorporated into the new bedrock layer. However, the grading of the new bedrock
390 layer remains unchanged although the material from the original soil layers two and three is
391 added to the bedrock layer. At the first glance it may seem that this process would drastically
392 alter the soilscape evolution dynamics by introducing a sharp contrast in soil grading at the
393 soil-bedrock interface. In SSSPAM a large number of soil layers (50 to 100) are used to ensure
394 smooth soil grading transition from soil to bedrock.

395 Figure 4 shows three different cases that can occur during the deposition process. In
396 Case 1 (Figure 4(b)) the deposition height Δh_D is less than the surface armour thickness D_{sur} .
397 In Case 2 (Figure 4(c)) the deposition height Δh_D is greater than the surface armour layer
398 thickness D_{sur} and the original surface armour layer is situated inside a single new subsurface
399 layer. Also the new soil subsurface layer which contains the original surface armour layer can
400 reside in any depth within new soil profile depending on the deposition height (e.g. it can be
401 1st, 2nd, 5th or any subsurface layer). For simplicity of explanation Figure 4(c) shows this layer
402 being in the 1st new subsurface layer. Case 3 (Figure 4(d)) is similar to the situation in Case 2
403 where the deposition height Δh_D is greater than the surface armour layer thickness D_{sur} .
404 However in this case the original surface armour layer belongs to two new subsurface layers
405 instead of one. As was with Case 2, the new soil subsurface layers, which contain portions of
406 the original surface armour layer, can reside at any depth within the new soil profile.
407 Calculation of soil grading of surface and all the subsurface soil layers are calculated with
408 different approaches according to previously mentioned deposition scenarios. A detailed
409 description of these soil grading approaches can be found in *Welivitiya* [2017].

410

411 2.4 Soil profile weathering

412 The methodology used for simulating weathering within the soil profile is detailed by
413 *Welivitiya et al.* [2016]. It uses a physical fragmentation mechanism where a parent particle
414 disintegrates into n number of daughter particles with a single daughter particle retaining
415 fraction α of the parent particle by volume and the remaining $n-1$ daughter particles retaining
416 fraction $1 - \alpha$ of the parent particle volume. By changing n and α we can simulate a wide
417 range of particle disintegration geometries which can be attributed to different weathering
418 mechanisms. In this paper we used $n = 2$ and $\alpha = 0.5$ to simulate symmetric fragmentation
419 mechanism where a single parent particle breaks down in to 2 equal daughter particles. But the
420 model can simulate any values of n and α which can simulate a wide range of weathering
421 mechanisms ranging from symmetric fragmentation to granular disintegration. We decided to
422 use the symmetric fragmentation mechanism based on the results of *Wells et al.* [2006]. Using
423 the above mentioned parameters, parent - daughter particle diameters and soil grading
424 distribution values, the weathering transition matrix is constructed according to the
425 methodology described by *Cohen et al.* [2009] and will not be discussed further.

426 The weathering rate of each soil layer is simulated using a depth dependent weathering
427 function. It defines the weathering rate as a function of the soil depth relative to the soil surface
428 depending on the mode of weathering of that particular material. SSSPAM can use different
429 depth depending weathering functions to simulate the soil profile weathering rate. For the
430 initial simulations presented in this paper we used the exponential [*Humphreys and Wilkinson,*
431 2007] and humped exponential [*Ahnert, 1977; Minasny and McBratney, 2006*] depth
432 dependent weathering functions. Detailed explanation and the rationale of these weathering
433 functions is presented in *Welivitiya et al.* [2016] and extended by Willgoose [2018].

434 It is important to note that SSSPAM can assign different weathering mechanisms (using
435 different values of n and α) and different depth dependent weathering functions for each pixel
436 (node) depending on the material and the dominant weathering drivers (such as temperature)
437 in the pixels geographical location. Also if need be, the depth dependent weathering function
438 at each pixel may be changed during the simulation to reflect any perceived temporal change
439 in weathering drivers by slightly modifying the weathering module. This will allow SSSPAM
440 to conduct simulation studies on global change incorporating both physical and chemical
441 weathering processes on soils in the future.

442 3 SSSPAM simulation setup

443 The objective of the simulations below was to explore the capabilities and implications
444 of the SSSPAM coupled soilscape-landform evolution model. Although the model is capable
445 of simulating soilscape and landform evolution for a three-dimensional catchment scale
446 landform, a synthetic two-dimensional linear hillslope (length and depth) landform was used
447 here. Because it is two-dimensional, the landform always discharges in a single direction. In
448 this way the complexities of multidirectional discharge were avoided so we can focus on the
449 soilscape-landform coupling.

450 The simulated landform starts from an almost flat 1 km long plateau (almost flat area
451 at the top of the hillslope) with a very small gradient of 0.001% (Figure 5). A hillslope with a
452 gradient of 2.1% starts at the edge of the plateau and continues 1.5 km horizontally while
453 dropping 31.5 m vertically and terminates at a valley. The valley (another almost flat area at
454 the bottom of the hillslope) itself has the same gradient as the upslope plateau (0.001%) and
455 continues for another 1 km. The valley (the bottom section of the landform) is designed to
456 facilitate sediment deposition so the effect of sediment deposition on soilscape development
457 can be analysed. The simulated hillslope has a constant width of 10 m (one pixel wide) and is
458 divided into 350, 10 m long pixels along slope. At each pixel the soil profile is defined by a
459 maximum of 102 soil layers. The soil surface armour layer is the topmost soil layer and it has
460 a thickness of 50 mm. The 100 layers below the surface layer are subsurface soil layers with a
461 thickness of 100 mm each. The bottommost layer (102nd layer) is a permanent non-weathering
462 layer and it is the limit of the hillslope modelling depth. In this way SSSPAM is capable of
463 modelling a soil profile with a maximum thickness of 10.05 m. By changing the number of soil
464 layers used in the simulation SSSPAM is able to simulate a soil profile with any thickness.
465 However as the number of model layers increases, the time required for the each simulation
466 also increases. During our initial testing, we found that the soil depth rarely increased beyond
467 10 m and decided to set 10.05 m as the maximum soil depth for this scenario.

468 Two soil grading data sets (Table 3) were used for the initial surface soil grading and
469 the bedrock. The first soil grading was from Ranger Uranium Mine (Northern Territory,
470 Australia) spoil site. This soil grading was first used by *Willgoose and Riley* [1998] for their
471 landform simulations. It was also subsequently used by *Sharmeen and Willgoose* [2007] for
472 their work with ARMOUR simulations and *Cohen et al.* [2009] for mARM simulation work.
473 The soil grading consisted of stony metamorphic rocks produced by mechanical weathering

474 with a body fracture mechanism [Wells et al., 2008]. It had a median diameter of 3.5 mm and
475 a maximum diameter of 19 mm (Table 3 - Ranger1a). The second grading was created to
476 represent the bedrock of the previous soil grading. It contained 100% of its mass in the largest
477 particle size class that is 19 mm (Table 3 - Ranger1b). These soil gradings are the same soil
478 gradings used in the SSSPAM parametric study of *Welivitiya et al.* [2016]. At the start of the
479 simulation the surface armour layer was set to the soil grading (Table 3 - Ranger1a) and all the
480 subsurface layers were set to bedrock grading (Table 3 - Ranger1b). The discharge (runoff
481 excess generation) rate of water is derived from averaging the 30 year rainfall data collected
482 by *Willgoose and Riley* [1998]. Using the simulation setup described above simulations was
483 carried out using the yearly averaged discharge rate. For this simulation we set the timestep to
484 10 years and the model was run for 10000 timesteps (simulating 100000 years of evolution).

485 **4 Simulation results with exponential weathering function**

486 Figure 6 shows six outputs at different times during hillslope and soil profile evolution.

487 The upper section in each of the panels in Figure 6 is the cross-section median diameter
488 (d_{50}) of the soil profile and the landform, with the line denoting the original landform surface.
489 The middle panel is the median diameter d_{50} of the soil surface armour layer. The bottom panel
490 is the soil profile relative to the surface highlighting the soil profile d_{50} (i.e elevation differences
491 at different nodes are removed and the d_{50} for all the nodes are displayed at the same level).
492 The soil depth is the depth below the surface at which d_{50} reaches the maximum possible
493 particle size (i.e. the bedrock grading). Figure 6(a) shows the initial condition for the soilscape:
494 a deep bedrock overlain by a very thin fine-grained soil layer. The evolution of the coupled
495 soilscape and landform at different simulation times are presented in subsequent Figures 6(b)
496 - 6(f).

497 If we initially consider the landform evolution alone, the erosion-dominated regions
498 and the deposition-dominated regions can be clearly identified. Initially erosion is highest on
499 top of the hillslope where the plateau transitions to the hillslope (plateau-hillslope boundary)
500 and erosion gradually reduces down the hillslope. Also, there is a sharp increase of surface d_{50}
501 at the plateau-hillslope boundary and then a gradual decrease down the hillslope. The summit
502 plateau has a very low slope gradient and although the contributing area increases across the
503 plateau, the potential erosion and the transport capacity of the flow remains negligible resulting
504 in minimum erosion. At the plateau-hillslope boundary, the slope gradient suddenly increases.
505 This increase in slope gradient and high contributing area increases the potential erosion of the

506 flow and causes a rapid increase in transport capacity downslope. This erosion gradually
507 reduces further down the hillslope despite increasing contributing area. Although the transport
508 capacity increases towards the bottom of the hillslope, water flowing over the downslope nodes
509 is laden with sediments already eroded from upslope nodes. This reduces the amount of erosion
510 at the downslope nodes.

511 Turning to the evolution of the soil profile, the upslope plateau retains the initial surface
512 soil layer without any armouring due to the very low erosion and it develops a relatively thick
513 soil profile as a result of bedrock weathering. The high erosion rate at the plateau-hillslope
514 boundary removes all the fine particles from the initial soil layer as well as fine particles
515 produced by weathering process, creating a very coarse surface armour layer. This high erosion
516 rate also leads to a relatively shallow soil profile. The erosion rate reduces down the slope due
517 to saturation of the flow with sediments from upstream. Low erosion leads to a weak armouring
518 and the fine particles produced from surface weathering remain on the surface. These processes
519 lead to the fining of the surface soil layer and thickening of the soil profile down the hillslope.

520 With time the location of the high erosion region shifts upstream onto the plateau
521 cutting into it. The d_{50} of the armour layer downslope also decreases. Both of these changes
522 occur due to lowering of the slope gradient of the hillslope over time.

523 Deposition of material occurs on either side of the hillslope-valley boundary. The valley
524 at the foot of the hillslope has a very low initial slope gradient. At the hillslope-valley boundary
525 (toe slope) the slope gradient reduces suddenly. This sudden slope gradient reduction reduces
526 the transport capacity of the water flow and initiates deposition. Initially deposition occurs only
527 at the hillslope-valley boundary node and increases its elevation. This deposition and slope
528 reduction propagates upslope until equilibrium is reached with erosion. Deposition propagates
529 across the valley and produces the deposits in Figure 6.

530 There is a change in surface d_{50} between the erosion and deposition regions starting at
531 around 2000 m. The surface d_{50} of the erosion region reduces down the slope, reaches a
532 minimum at 2000 m and then increases as it transitions into the deposition region. This can be
533 clearly seen in Figures 6(c) and 6(d). As noted previously the “actual erosion rate” reduces
534 down the slope due to saturation of the flow with sediments. At the end of the erosion region
535 no more erosion can take place because the flow is completely saturated with sediment.
536 Because of the lack of erosion, fine particles are not removed from the surface and weathering
537 produces more and more fine particles reducing the surface d_{50} and increasing the soil depth.

538 Near the erosion-deposition boundary, only a small amount of sediment is deposited.
539 Since the larger particles have the highest probability of deposition, a small amount of coarse
540 material deposits there. Downslope into the deposition region the slope further decreases, the
541 difference between the transport capacity and the sediment load increases and the rate of
542 deposition steadily increases. Since larger particles have a higher probability of depositing first,
543 coarse material preferentially deposits. Mixing of these coarse particles with pre-existing
544 weathered fine particles produces the observed coarsening of the surface d_{50} . Once the surface
545 d_{50} of the deposition region reaches a peak it starts to decrease again (from 2500 m to 3000 m).
546 Beyond 3000 m the deposited material is smaller because the larger particles have already been
547 deposited upstream. The deposition of each consecutive downstream node consists with finer
548 particles leading to the observed decrease of surface and profile d_{50} . As expected the soil
549 thickness is higher in the deposition regions than the other regions.

550 With time the deposition region moves upslope. The gradient of d_{50} observed in earlier
551 times of the deposition region (until 30,000 years) decreases and the soil changes into a very
552 fine-grained homogeneous material resulting from surface weathering. Due to the high
553 weathering rate at the surface and the upper soil layers, the deposited sediment decomposes
554 into a very fine material. With time, the d_{50} of the sediments in the water flow also decreases
555 due to low erosion potential and weathering of the surface armour layer of upslope nodes. For
556 these reasons the d_{50} of the deposition region decreases and becomes homogeneous leading to
557 burial of the coarse material that was deposited earlier.

558 The simulation produced a landform morphology which resemble the five unit model
559 proposed by *Ruhe and Walker* [1968]. At the conclusion of the simulation the plateau area
560 resembles a flat summit, the plateau-hillslope boundary resembles the convex shoulder,
561 transition region from the plateau-hillslope boundary to the deposition region resembles the
562 backslope with a uniform slope, and the deposition region resembles the concave base divided
563 in to upper footslope and lower toeslope. Generally the soil grading distribution is fine at the
564 summit, coarsens from the summit to the shoulder and backslope followed by fining from
565 backslope to the base [*Birkeland*, 1984]. Furthermore, the soil depth is typically high in summit
566 area, low in shoulder and blacslope, high in upper footslope and lower toeslope [*Brunner et al.*,
567 2004]. The soil grading and the soil depth variations of our simulations produces similar trends.

568 **4.1 Evolution characteristics of different sites**

569 In order to better understand the dynamics of soilscape evolution we also plotted the
570 elevation, slope, rate of erosion (and/or deposition), surface d_{50} , soil depth and profile d_{50} for
571 four sites (Figure 6(a)). The first two sites (sites 1 and 2) are either side of the plateau-hillslope
572 boundary in the erosion region. The other two sites (sites 3 and 4) are either side of the
573 hillslope-valley boundary in the deposition region.

574 ***Site 1 and 2:***

575 For site 1 (Figure 7- solid line plots) the erosion and surface d_{50} are strongly correlated
576 over time. The soil depth and profile d_{50} plots are also highly correlated. The abrupt change in
577 profile d_{50} occurs at the same time as abrupt changes in soil depth. Site 1 initially has small
578 erosion because the slope is very low. This small amount of erosion means the elevation and
579 slope are initially constant. Due to the dominance of weathering, both surface and profile
580 grading become enriched with fine particles and the d_{50} decreases. Weathering of the profile
581 layers creates a relatively deep soil profile. With time the erosion front, initially at the plateau-
582 hillslope transition, cuts back into the plateau. The increased erosion rate removes the fine
583 material created by weathering leading to a coarse-grained armour. This observation may have
584 some important implications for the landform evolution modelling community. Most landform
585 evolution models which does not explicitly model soil profile evolution or weathering
586 considers a single unchanging soil layer on top of the landform. When evolving a landform
587 similar to the setup used in this manuscript, such landform evolution models may underestimate
588 upward propagation rate of the erosion front as they will be trying to erode relatively coarser
589 particles. With weathering producing smaller particles the erosion front would propagate faster
590 in a natural hillslope.

591 When the erosion front crosses site 1, the gradient increases as does the erosion rate (at
592 around 20,000 years). During this phase of increasing erosion the surface d_{50} also increased.
593 However, the surface d_{50} stabilizes around 14 mm before the erosion rate reaches its maximum
594 value. This is because once total armouring occurs, the erosion is reduced to a very low value.
595 Although the erosion is low, the slope of the site 1 continues to increase until it reaches a
596 maximum and the Shield's shear stress threshold diameter also increases. This allows erosion
597 to keep increasing while the surface d_{50} remain essentially constant. When the erosion rate
598 overtakes the rate of production of weathering, the soil depth decreases. Increasing erosion
599 reduces the soil thickness while coarsening the surface of upper soil layers. This results in the
600 increase of the profile d_{50} at later times. At 20,000 years, the reduction of slope reduces the rate

601 of erosion so that, weathering again dominates the site. Weathering produces more fine
602 particles reducing the surface d_{50} from about 48,000 years. The dominance of weathering over
603 erosion also increases the soil depth while decreasing the profile d_{50} .

604 Both soil depth and profile d_{50} plots resemble a stair-stepped graph. The reason for this
605 appearance is that SSSPAM calculates soil depths as the number soil profile layers. The model
606 doesn't interpolate the depth of soil within a single layer. Since the profile d_{50} is a function the
607 soil thickness, this plot also displays this pattern.

608 For site 2 (Figure 7-dashed line plots) the evolution is simpler than site 1. The initial
609 transport capacity and discharge energy at site 2 is very high while the sediment inflow from
610 upstream is low because of low erosion from the plateau. The resulting higher erosion rate
611 produces a very coarse surface layer and exposes the bedrock in the subsurface. This effect
612 causes both the surface d_{50} and profile d_{50} to rapidly increase to the maximum possible diameter
613 (bedrock grading).

614 Although the surface d_{50} has reached the maximum possible diameter the erosion
615 continues to increase as the Shield's threshold diameter for entrainment of the water flow has
616 increased beyond the maximum particle size (19 mm) and the bedrock grading itself is being
617 eroded. However, at around 2,700 years the Shield's threshold diameter decreases below 19
618 mm and the fully armoured surface causes the erosion rate to decrease rapidly and becomes
619 unstable in time with rapid fluctuations. Once an armour layer develops on the surface, the
620 profile layers are protected from erosion and weathering becomes more dominant, so the profile
621 d_{50} decreases while soil depth increase.

622 ***Site 3 and 4:***

623 For site 3 (Figures 8-solid line plots) the elevation increases due to deposition. The
624 initial increase of surface d_{50} occurs due to size selective deposition. As noted in the model
625 description, larger particles deposit at a higher rate. This deposition of larger particles on the
626 surface causes the surface d_{50} to initially increase.

627 The subsequent decrease of the surface d_{50} occurs due to a combination of two
628 processes. Firstly, with time the upstream boundary of the deposition region moves upslope
629 and since the largest particles tend to deposit at the beginning of the deposition region, the
630 sediment flow at site 3 gets enriched with more and more fine particles. Due to the deposition
631 of these relatively finer particles the surface d_{50} tends to decrease. Secondly, weathering of the

632 surface and the subsurface layers reduces the surface d_{50} . Compared to sites 1 and 2 the soil
633 depth increase of site 3 is much higher. In sites 1 and 2 the soil profile growth only occurred
634 due to the excess of weathering over erosion. At site 3 the soil layer grows due to material
635 deposition as well as weathering of the bedrock. The profile d_{50} increases in the initial stage.

636 For site 4 (Figures 8-dashed line plots) while the initial evolution is different, in the
637 latter stages (beyond year 15,000) the evolution characteristics of the soil properties are similar
638 to that of site 3. Since the valley initially has a low slope, the initial erosion is negligible and
639 the elevation, slope and erosion remain close to 0. With the growth of the deposition region, a
640 “deposition front” moves across the valley. Before the deposition front reaches site 4, the
641 elevation, slope and erosion/deposition remain unchanged. Because the initial erosion rate at
642 site 4 is low, there is no armouring so that weathering dominates and the surface d_{50} decreases.
643 When the deposition front reaches site 4, the elevation increases due to sediment deposition as
644 so does the slope. Due to the size selective deposition of coarse sediment the surface d_{50}
645 increases. Afterwards the evolution of the soil properties is similar to site 3 as the same
646 processes are acting at sites 3 and 4.

647 **5 Simulation results with humped exponential weathering function**

648 To test the sensitivity of the conclusions in the previous section to changes in the depth
649 dependent weathering functions, in this section we explore the effect of weathering using the
650 humped exponential weathering function. The key difference is that the humped function has
651 a low weathering rate at the surface with the peak weathering rate occurring mid-profile.

652 Superficially, both the humped and exponential weathering functions produce similar
653 trends, however there are some differences in the particle size distribution, soil depth and the
654 evolution of the landform (Figure 9). At identical times the surface d_{50} is coarser and the soil
655 depth is less for the humped simulations. There is also a subtle difference in the initial landform
656 evolution. For the exponential weathering function the highest erosion rate occurs near the
657 plateau-hillslope boundary (year 2000 near 1,000 m, Figure 6). For the humped function this
658 maximum soil surface deviation occurs further down the hillslope (year 2000 near 1500 m,
659 Figure 9). For subsequent times, this difference in the location of the maximum erosion leads
660 to subtly different landforms.

661 These differences in landform evolution are explained by the near surface weathering
662 rates. For the exponential weathering function the weathering rate is highest at the surface and

663 declines exponentially with depth. For the humped exponential weathering function the highest
664 weathering rate is at a finite depth below the surface and exponentially decrease below and
665 above this depth. Because of the lower surface weathering rate for humped, the surface d_{50}
666 remains coarser during the entire simulation. The relative coarseness of the surface means that
667 the water flow needs to be more energetic to entrain material from the surface due to the
668 Shields's stress entrainment threshold. For the exponential weathering function simulations,
669 shear stress of the water flow is high enough to entrain most of the surface soil particles near
670 the plateau-hillslope boundary owing to the finer armour layer as a result of surface weathering.
671 However for the humped exponential weathering simulations the surface armour is coarser
672 because of the lower surface weathering rate and the shear stress of the water flow is not high
673 enough to detach material from the armour layer. Because of this, the highest erosion occurs
674 downslope where the contributing area is higher and hence the shear stress of the water flow is
675 higher.

676 **6 Model and simulation limitations**

677 Currently the coupled soilscape-landform evolution model SSSPAM presented here is
678 limited in its scientific scope. The model is based on physical fragmentation of parent soil
679 particles and it does not model chemical transformations. Also at the current time SSSPAM
680 does not account for Soil Organic Carbon (SOC) and its influence in the soil formation and
681 evolution processes. The modelling approach used here is complimentary to the chemical
682 weathering modelling work done by Kirkby [Kirkby, 1977; 1985; 2018]. However we will be
683 incorporating a physically based chemical weathering model described by Willgoose [2018]
684 into SSSAPAM in the future. All available evidence suggests that in order to effectively model
685 SOC, it will require an extremely complicated coupled model which requires soil grading, soil
686 moisture as well as vegetation and decomposition rates. Although formulating such a model is
687 very desirable (and would be an important endeavour by itself) for the entire scientific
688 community, it is well beyond the scope of this current research work.

689 The deposition model of SSSPAM is designed in such a way that the difference between
690 the transport capacity and the sediment load of the flow is always deposited regardless of the
691 settling velocities. This is done to prevent the flow from being over the transport capacity.
692 Depending on the material grading distribution and the concentration in the profile of the flow,
693 the theoretical amount of the material that can be deposited can be different. In this model
694 formulation we assume that the sediment grading is uniform and the sediment concentration is

695 also uniform within the flow. The reality may not be as simple as that. There are some literature
696 such as Agrawal et al. [2012] which argue that the sediment concentration profile has an
697 exponential distribution (i.e. most of the sediment are concentrated near the bottom of the flow)
698 and that the grading distribution profile in the flow is also a function of the settling velocity of
699 different particles (i.e. Larger particles are concentrated near the bottom of the flow). So in
700 practice the amount of material deposited at each pixel according to the critical immersion
701 depth might be higher. Although the approach used in SSSPAM may not perfectly mimic the
702 natural behaviour of sediment deposition, we believe that this is an effective way to numerically
703 represent this process in the model at this time.

704 The main objective of this manuscript was to introduce the new coupled soilscape-
705 landform evolution model. Here some applications of the model simulations albeit simple was
706 presented to show how the model performed in reality and to highlight some of the geomorphic
707 signatures emerging from the modelling results itself. The simulation setup may not be a
708 reasonable application that necessarily reflects the total environment. However we are inspired
709 by the early work on hillslope geomorphology by authors such as Kirkby [1971] and Carson
710 and Kirkby [1972] which was very useful in understanding hillslope evolution processes. So
711 as a first step we used a one-dimensional hillslope to run our simulations because,
712 understanding dynamics of 1D hillslope evolution is simpler and we can better illustrate
713 possible implications for different processes. Further, only limited comparison with field data
714 was possible because of a dearth of any experimental work done by other researchers using.
715 However a subsequent paper will deal with implications of model results in terms of one-
716 dimensional and three-dimensional alluvial fans. In this future manuscript, we compare and
717 contrast the model results with experimental work done by authors like Seal et al. [1997], Toro-
718 Escobar et al. [2000] and general observation done regarding naturally occurring alluvial fans
719 and their formation dynamics.

720 **7 Conclusions**

721 This study presents a methodology for incorporating landform evolution into the
722 SSSPAM soil grading evolution model. This was achieved by incorporating elevation changes
723 produced by erosion and deposition. Previous published work with SSSPAM assumed that the
724 landform, slope gradients and contributing areas remained constant during the simulation. This
725 did not preclude the landform evolving, only that the soil reached equilibrium faster (i.e. had a
726 shorter response time) than the landform evolved (i.e. a “fast” soil, Willgoose, 2018). In the

727 new version of SSSPAM discussed here, the elevations, contributing area, slope gradient and
728 slope directions at each node dynamically evolve. This new model explicitly models co-
729 evolution of the soil and the landform, where the response time for soil and landform are
730 similar.

731 By defining “the critical immersion depth”, a novel and simple methodology for size
732 selective deposition was introduced to formulate the deposition transition matrix. This
733 deposition transition matrix characterises the size selectivity of sediment deposition depending
734 on the settling velocity of the sediment particle, with faster settling velocity particles settling
735 first.

736 The results demonstrated SSSPAM’s ability to simulate erosion, deposition and
737 weathering processes which govern soil formation and its evolution coupled with an evolving
738 landform. The simulation results qualitatively agree with general trends in soil catena observed
739 in the field. The model predicts the development of a thin and coarse-grained soil profile on
740 the upper eroding hillslope and thick and fine-grained soil profile at the bottom valley.
741 Considering the dominant process acting upon the soilscape, the hillslope can be divided into
742 weathering-dominated, erosion-dominated and deposition-dominated sections. The plateau
743 (summit) was mainly weathering-dominated due to its very low slope gradient and low erosion
744 rate. The upper part of the hillslope was erosion-dominated owing to its high slope gradient
745 and high contributing area. The lower part of the hillslope and the valley was deposition-
746 dominated. The position and the size of these sections changes with time due to the evolution
747 of the landform and the soil profile. During the simulation, the weathering-dominated region
748 shrinks due to the erosional region dominating it. The erosion-dominated region expands
749 upslope into the previously weathering-dominated region and the downstream boundary
750 retreats upslope away from the deposition-dominated region, but shows a net expansion in area.
751 The deposition-dominated region expands upslope into the previously erosion-dominated
752 region with a net expansion.

753 The simulation results also show how the interaction of different processes can have
754 unexpected outcomes in terms of soilscape evolution. The best example is the fining of the
755 surface grading despite an increasing transport capacity and potential erosion rate. This occurs
756 due to saturation of the flow with sediment eroded from upstream nodes. Further, the
757 comparison of results produced by the exponential and humped exponential weathering
758 functions showed how the distribution of weathering rate down the soil profile changes the

759 overall properties of the soilscape. For instance, the humped exponential simulation produced
760 a thinner soil profile and coarser soil surface armour compared with simulation results of
761 exponential weathering function because of the reduced weathering rate at the soil surface. This
762 led to a longer-lived surface armour for the humped function.

763 The synthetic landform simulations demonstrated SSSPAM's ability to qualitatively
764 simulate erosion, deposition and weathering processes and to generate familiar soilscape
765 observed in the field. Comparison of results obtained from two different depth different
766 functions demonstrate how the soilscape dynamic evolution is influenced by the weathering
767 mechanisms. This in turn links to the geology of the soil parent material and their preferred
768 weathering mechanism which leads to the heterogeneity of soilscape properties in a region. A
769 future paper will discuss how this work can be extended to include the impact of chemical
770 weathering into soilscape evolution.

771 **7 References**

772 Agrawal, Y. C., O. A. Mikkelsen, and H. Pottsmith (2012), Grain size distribution and sediment flux
773 structure in a river profile, measured with a LISST-SL Instrument, *Sequoia Scientific, Inc. Report*.

774
775 Ahnert, F. (1977), Some comments on the quantitative formulation of geomorphological processes in
776 a theoretical model, *Earth Surface Processes*, 2(2-3), 191-201, doi:10.1002/esp.3290020211.

777
778 Arya, L. M., and J. F. Paris (1981), A physicoempirical model to predict the soil moisture characteristic
779 from particle-size distribution and bulk density data, *Soil Sci. Soc. Am. J.*, 45(6), 1023-1030.

780
781 Behrens, T., and T. Scholten (2006), Digital soil mapping in Germany—a review, *Journal of Plant*
782 *Nutrition and Soil Science*, 169(3), 434-443, doi:10.1002/jpln.200521962.

783
784 Benites, V. M., P. L. O. A. Machado, E. C. C. Fidalgo, M. R. Coelho, and B. E. Madari (2007), Pedotransfer
785 functions for estimating soil bulk density from existing soil survey reports in Brazil, *Geoderma*, 139(1–
786 2), 90-97, doi:<http://dx.doi.org/10.1016/j.geoderma.2007.01.005>.

787
788 Birkeland, P. W. (1984), *Soils and geomorphology*, Oxford University Press.

789
790 Brunner, A. C., S. J. Park, G. R. Ruecker, R. Dikau, and P. L. G. Vlek (2004), Catenary soil development
791 influencing erosion susceptibility along a hillslope in Uganda, *CATENA*, 58(1), 1-22,
792 doi:<http://dx.doi.org/10.1016/j.catena.2004.02.001>.

793
794 Bryan, R. B. (2000), Soil erodibility and processes of water erosion on hillslope, *Geomorphology*, 32(3–
795 4), 385-415, doi:[http://dx.doi.org/10.1016/S0169-555X\(99\)00105-1](http://dx.doi.org/10.1016/S0169-555X(99)00105-1).

796
797 Carson, M. A., and M. J. Kirkby (1972), Hillslope form and process.

798 Chittleborough, D. (1992), Formation and pedology of duplex soils, *Animal Production Science*, 32(7),
799 815-825.

800

801 Cohen, S., G. Willgoose, and G. Hancock (2009), The mARM spatially distributed soil evolution model:
802 A computationally efficient modeling framework and analysis of hillslope soil surface organization, *J.*
803 *Geophys. Res.-Earth Surf.*, *114*, doi:F0300110.1029/2008jf001214.

804 Cohen, S., G. Willgoose, and G. Hancock (2010), The mARM3D spatially distributed soil evolution
805 model: Three-dimensional model framework and analysis of hillslope and landform responses, *J.*
806 *Geophys. Res.-Earth Surf.*, *115*, doi:F0401310.1029/2009jf001536.

807 Coon, W. F. (1998), *Estimation of roughness coefficients for natural stream channels with vegetated*
808 *banks*, US Geological Survey.

809
810 Gessler, P. E., O. Chadwick, F. Chamran, L. Althouse, and K. Holmes (2000), Modeling soil–landscape
811 and ecosystem properties using terrain attributes, *Soil Sci. Soc. Am. J.*, *64*(6), 2046-2056.

812
813 Gessler, P. E., I. Moore, N. McKenzie, and P. Ryan (1995), Soil-landscape modelling and spatial
814 prediction of soil attributes, *International Journal of Geographical Information Systems*, *9*(4), 421-432.

815
816 Hillel, D. (1982), *Introduction to soil physics*, Academic Press.

817
818 Hoosbeek, M. R., and R. B. Bryant (1992), TOWARDS THE QUANTITATIVE MODELING OF PEDOGENESIS
819 - A REVIEW, *Geoderma*, *55*(3-4), 183-210, doi:10.1016/0016-7061(92)90083-j.

820
821 Humphreys, G. S., and M. T. Wilkinson (2007), The soil production function: A brief history and its
822 rediscovery, *Geoderma*, *139*(1–2), 73-78, doi:<http://dx.doi.org/10.1016/j.geoderma.2007.01.004>.

823
824 Jenny, H. (1941), *Factors of soil formation*, McGraw-Hill Book Company New York, NY, USA.

825
826 Kirkby, M. (1971), Hillslope process-response models based on the continuity equation, *Inst. Br. Geogr.*
827 *Spec. Publ*, *3*(1), 5-30.

828
829 Kirkby, M. (1977), Soil development models as a component of slope models, *Earth surface processes*,
830 *2*(2-3), 203-230.

831
832 Kirkby, M. (1985), A basis for soil profile modelling in a geomorphic context, *Journal of Soil Science*,
833 *36*(1), 97-121.

834
835 Kirkby, M. (2018), A conceptual model for physical and chemical soil profile evolution, *Geoderma*.

836
837 Lerman, A. (1979), *Geochemical processes. Water and sediment environments*, John Wiley and Sons,
838 Inc.

839
840 Lin, H. (2011), Three Principles of Soil Change and Pedogenesis in Time and Space, *Soil Sci. Soc. Am. J.*,
841 *75*(6), 2049-2070, doi:10.2136/sssaj2011.0130.

842
843 McBratney, A. B., M. L. Mendonça Santos, and B. Minasny (2003), On digital soil mapping, *Geoderma*,
844 *117*(1–2), 3-52, doi:[http://dx.doi.org/10.1016/S0016-7061\(03\)00223-4](http://dx.doi.org/10.1016/S0016-7061(03)00223-4).

845
846 Meyer-Peter, E., and R. Müller (1948), Formulas for bed-load transport, IAHR.

847
848 Minasny, B., and A. B. McBratney (1999), A rudimentary mechanistic model for soil production and
849 landscape development, *Geoderma*, *90*(1-2), 3-21, doi:10.1016/s0016-7061(98)00115-3.

850 Minasny, B., and A. B. McBratney (2006), Mechanistic soil-landscape modelling as an approach to
851 developing pedogenetic classifications, *Geoderma*, 133(1-2), 138-149,
852 doi:10.1016/j.geoderma.2006.03.042.
853

854 O'Callaghan, J. F., and D. M. Mark (1984), The extraction of drainage networks from digital elevation
855 data, *Computer vision, graphics, and image processing*, 28(3), 323-344.
856

857 Parker, G., and P. C. Klingeman (1982), On why gravel bed streams are paved, *Water Resources*
858 *Research*, 18(5), 1409-1423, doi:10.1029/WR018i005p01409.
859

860 Rickenmann, D. (1994), An alternative equation for the mean velocity in gravel-bed rivers and
861 mountain torrents, paper presented at Proceedings of the ASCE National Conference on Hydraulic
862 Engineering.
863

864 Ruhe, R. V., and P. Walker (1968), Hillslope models and soil formation. I. Open systems, *Int Soc Soil Sci*
865 *Trans*.
866

867 Salvador-Blanes, S., B. Minasny, and A. B. McBratney (2007), Modelling long-term in situ soil profile
868 evolution: application to the genesis of soil profiles containing stone layers, *European Journal of Soil*
869 *Science*, 58(6), 1535-1548, doi:10.1111/j.1365-2389.2007.00961.x.
870

871 Schaap, M. G., F. J. Leij, and M. T. van Genuchten (2001), rosetta: a computer program for estimating
872 soil hydraulic parameters with hierarchical pedotransfer functions, *J. Hydrol.*, 251(3-4), 163-176,
873 doi:[http://dx.doi.org/10.1016/S0022-1694\(01\)00466-8](http://dx.doi.org/10.1016/S0022-1694(01)00466-8).
874

875 Scull, P., J. Franklin, O. Chadwick, and D. McArthur (2003), Predictive soil mapping: a review, *Progress*
876 *in Physical Geography*, 27(2), 171-197.
877

878 Seal, R., C. Paola, G. Parker, J. B. Southard, and P. R. Wilcock (1997), Experiments on downstream fining
879 of gravel: I. Narrow-channel runs, *Journal of hydraulic engineering*, 123(10), 874-884.
880

881 Sharmeen, S., and G. R. Willgoose (2006), The interaction between armouring and particle weathering
882 for eroding landscapes, *Earth Surface Processes and Landforms*, 31(10), 1195-1210,
883 doi:10.1002/esp.1397.
884

885 Sharmeen, S., and G. R. Willgoose (2007), A one-dimensional model for simulating armouring and
886 erosion on hillslopes: 2. Long term erosion and armouring predictions for two contrasting mine spoils,
887 *Earth Surface Processes and Landforms*, 32(10), 1437-1453, doi:10.1002/esp.1482.
888

889 Sommer, M., H. Gerke, and D. Deumlich (2008), Modelling soil landscape genesis—a “time split”
890 approach for hummocky agricultural landscapes, *Geoderma*, 145(3), 480-493.
891

892 Strahler, A. H., and A. N. Strahler (2006), *Introducing physical geography*, J. Wiley.
893 Tarboton, D. G. (1997), A new method for the determination of flow directions and upslope areas in
894 grid digital elevation models, *Water resources research*, 33(2), 309-319.
895

896 Temme, A. J., and T. Vanwallegem (2015), LORICA—A new model for linking landscape and soil profile
897 evolution: Development and sensitivity analysis, *Computers & Geosciences*.
898

899 Toro-Escobar, C. M., C. Paola, G. Parker, P. R. Wilcock, and J. B. Southard (2000), Experiments on
900 downstream fining of gravel. II: Wide and sandy runs, *Journal of Hydraulic Engineering*, 126(3), 198-
901 208.

902

903 Vanwalleghem, T., U. Stockmann, B. Minasny, and A. B. McBratney (2013), A quantitative model for
904 integrating landscape evolution and soil formation, *Journal of Geophysical Research: Earth Surface*,
905 118(2), 331-347, doi:10.1029/2011JF002296.

906

907 Welivitiya, W. D. D. P. (2017), A next generation spatially distributed model for soil profile dynamics
908 and pedogenesis, University of Newcastle, Australia, University of Newcastle, Australia.

909

910 Welivitiya, W. D. D. P., G. R. Willgoose, G. R. Hancock, and S. Cohen (2016), Exploring the sensitivity
911 on a soil area-slope-grading relationship to changes in process parameters using a pedogenesis model,
912 *Earth Surf. Dynam.*, 4(3), 607-625, doi:10.5194/esurf-4-607-2016.

913

914 Wells, T., P. Binning, G. Willgoose, and G. Hancock (2006), Laboratory simulation of the salt weathering
915 of schist: I. Weathering of schist blocks in a seasonally wet tropical environment, *Earth Surface
916 Processes and Landforms*, 31(3), 339-354, doi:10.1002/esp.1248.

917

918 Willgoose, G. (2018), *Principles of Soilscape and Landscape Evolution*, Cambridge University Press.

919

920 Willgoose, G., R. L. Bras, and I. Rodriguez-Iturbe (1991), A coupled channel network growth and
921 hillslope evolution model: 1. Theory, *Water Resources Research*, 27(7), 1671-1684,
922 doi:10.1029/91wr00935.

923

924 Willgoose, G., and S. Riley (1998), The long-term stability of engineered landforms of the Ranger
925 Uranium Mine, Northern Territory, Australia: Application of a catchment evolution model, *Earth Surf.
926 Process. Landf.*, 23(3), 237-259, doi:10.1002/(sici)1096-9837(199803)23:3<237::aid-esp846>3.0.co;2-
927 x.

928

929 Willgoose, G., and S. Sharmeen (2006), A One-dimensional model for simulating armouring and
930 erosion on hillslopes: I. Model development and event-scale dynamics, *Earth Surface Processes and
931 Landforms*, 31(8), 970-991, doi:10.1002/esp.1398.

932

933 Yoo, K., and S. M. Mudd (2008), Toward process-based modeling of geochemical soil formation across
934 diverse landforms: A new mathematical framework, *Geoderma*, 146(1-2), 248-260,
935 doi:<http://dx.doi.org/10.1016/j.geoderma.2008.05.029>.

936

937 Zhang, G.-H., L.-L. Wang, K.-M. Tang, R.-T. Luo, and X. Zhang (2011), Effects of sediment size on
938 transport capacity of overland flow on steep slopes, *Hydrological Sciences Journal*, 56(7), 1289-1299.

939

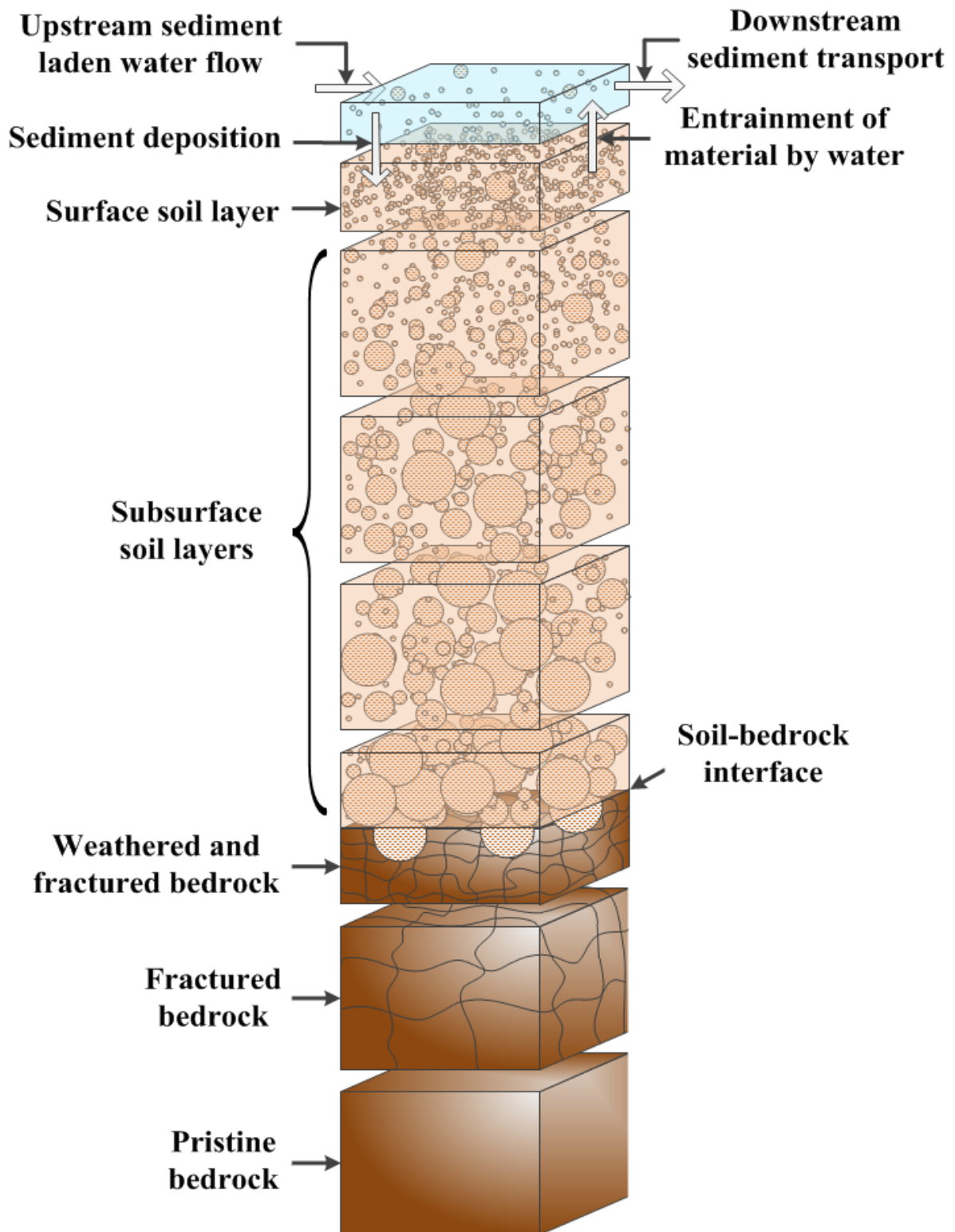
940

941

942

943

Figure 1



945

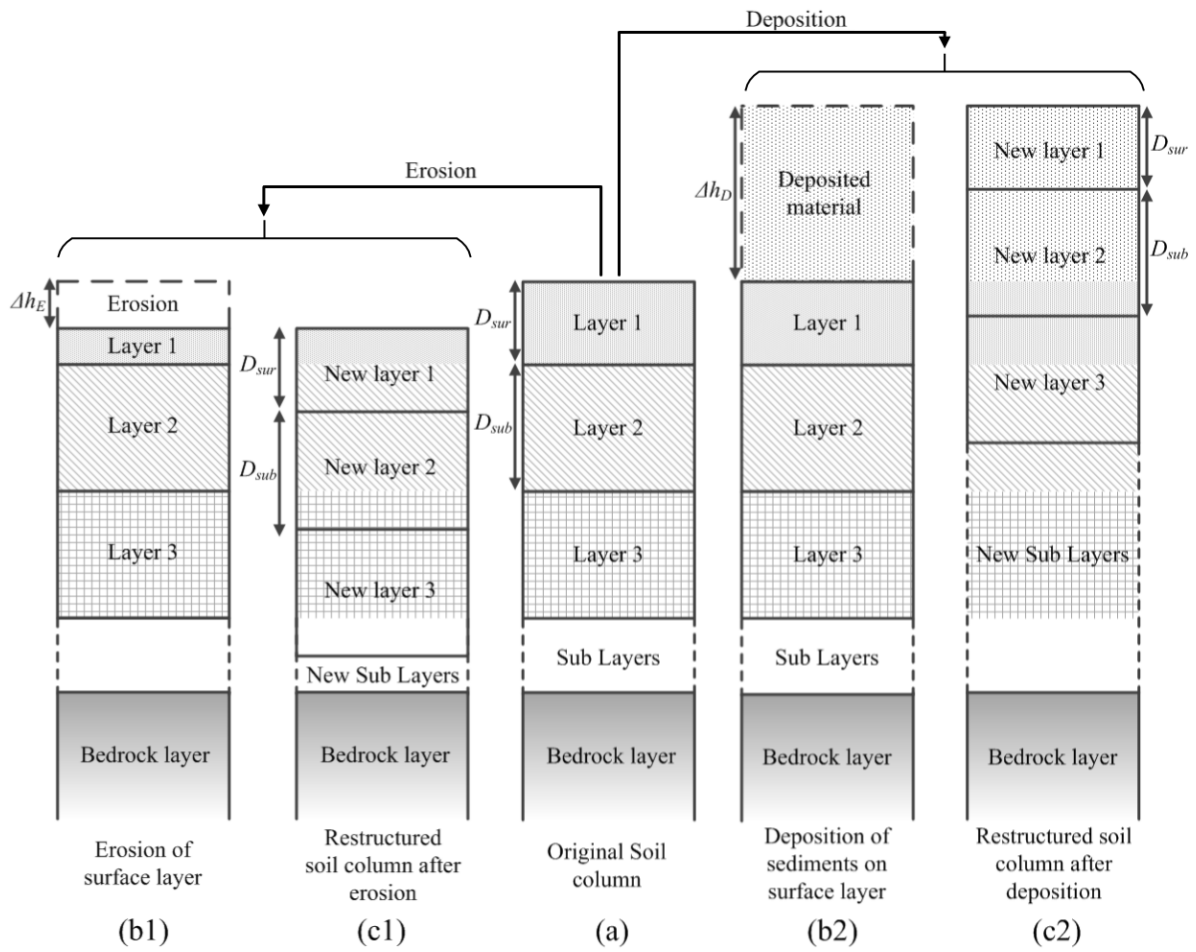
946

Figure 1 Schematic diagram of the SSSPAM model.

947

948

Figure 2



950

951 **Figure 2** Erosion, Deposition and the restructuring of the soil profile (a) original soil profile,
 952 (b1, c1) for erosion, (b2, c2) for deposition.

953

954

955

956

957

958

959

960

961

962

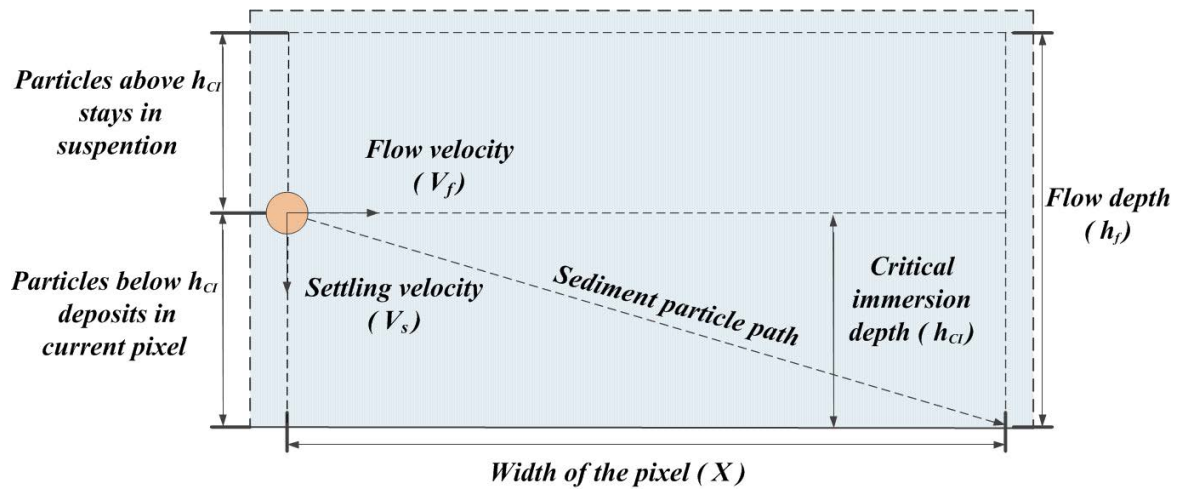
963

964

965

966

Figure 3



967

968

Figure 3 Determination of critical immersion depth of a sediment particle

969

970

971

972

973

974

975

976

977

978

979

980

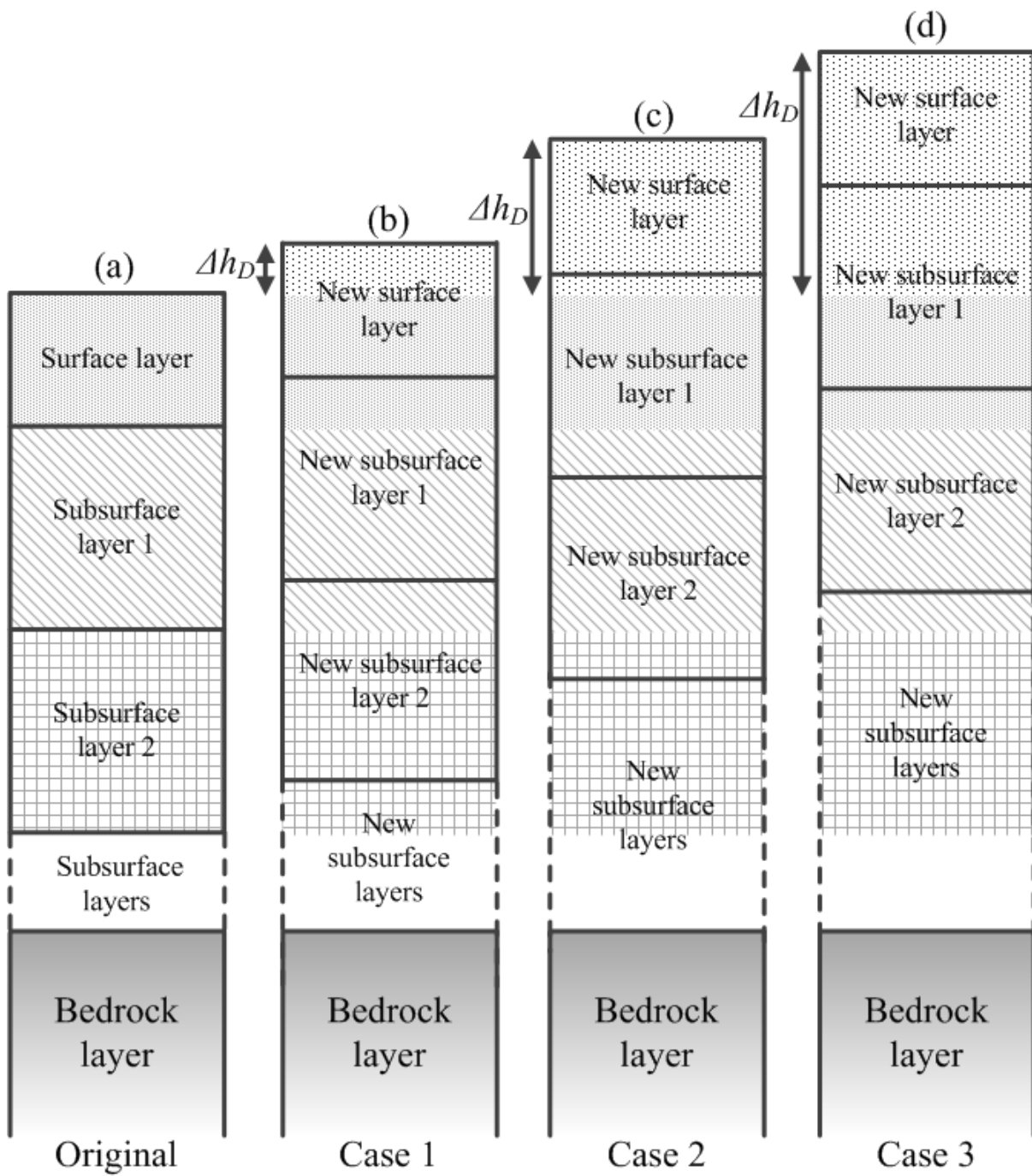
981

982

983

984

Figure 4



985

986

987

988

989

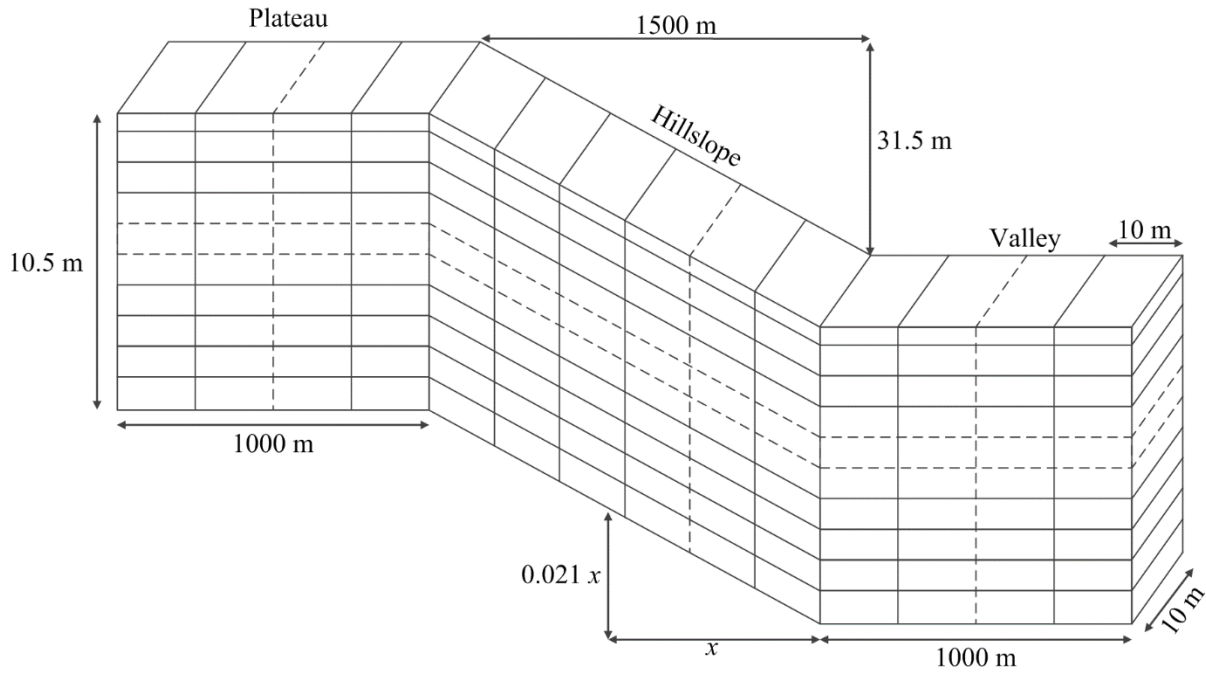
Figure 4 Different deposition scenarios

990

991

992

Figure 5



993

994

Figure 5 The simulated landform and the definition of nodes.

995

996

997

998

999

1000

1001

1002

1003

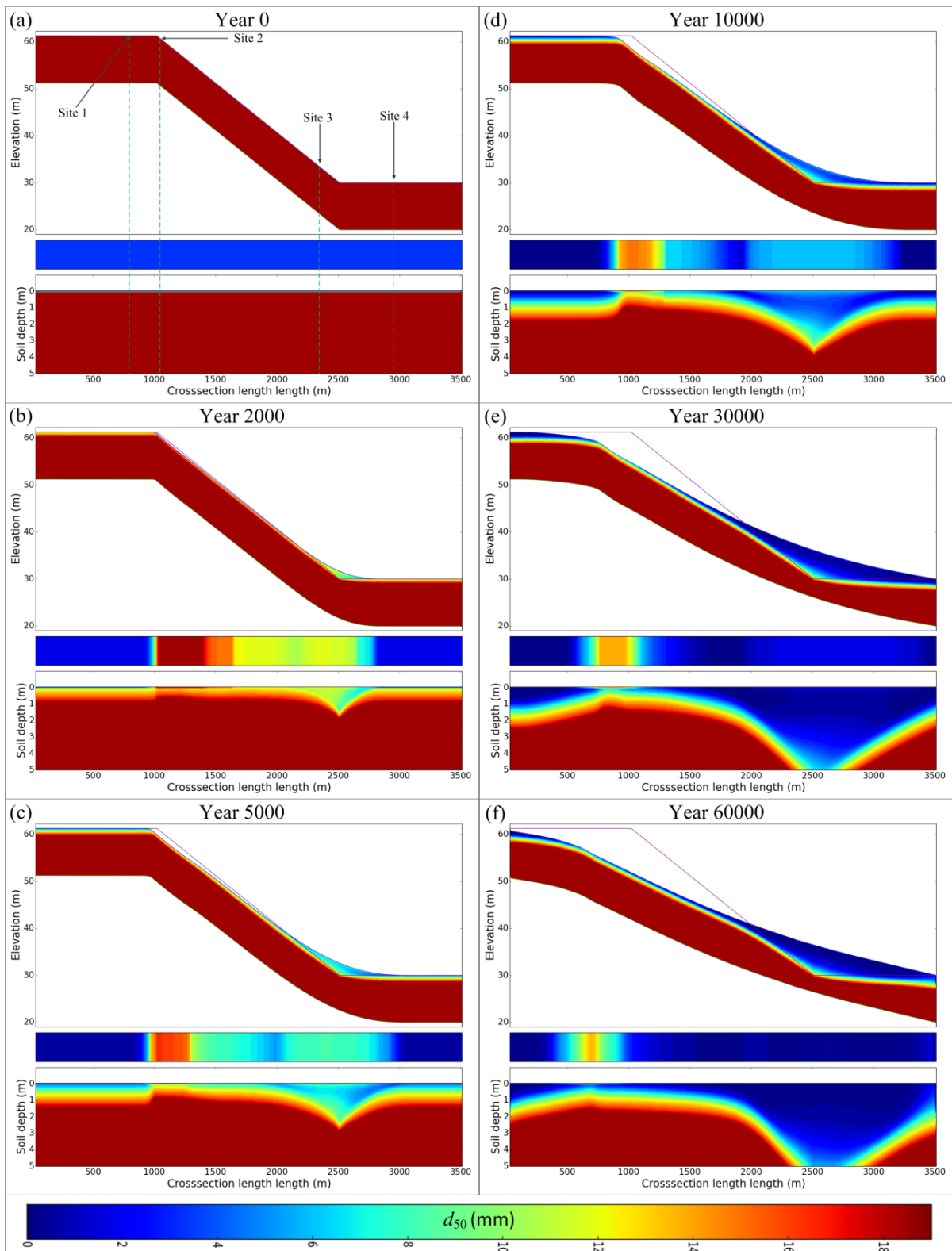
1004

1005

1006

1007

Figure 6



1009

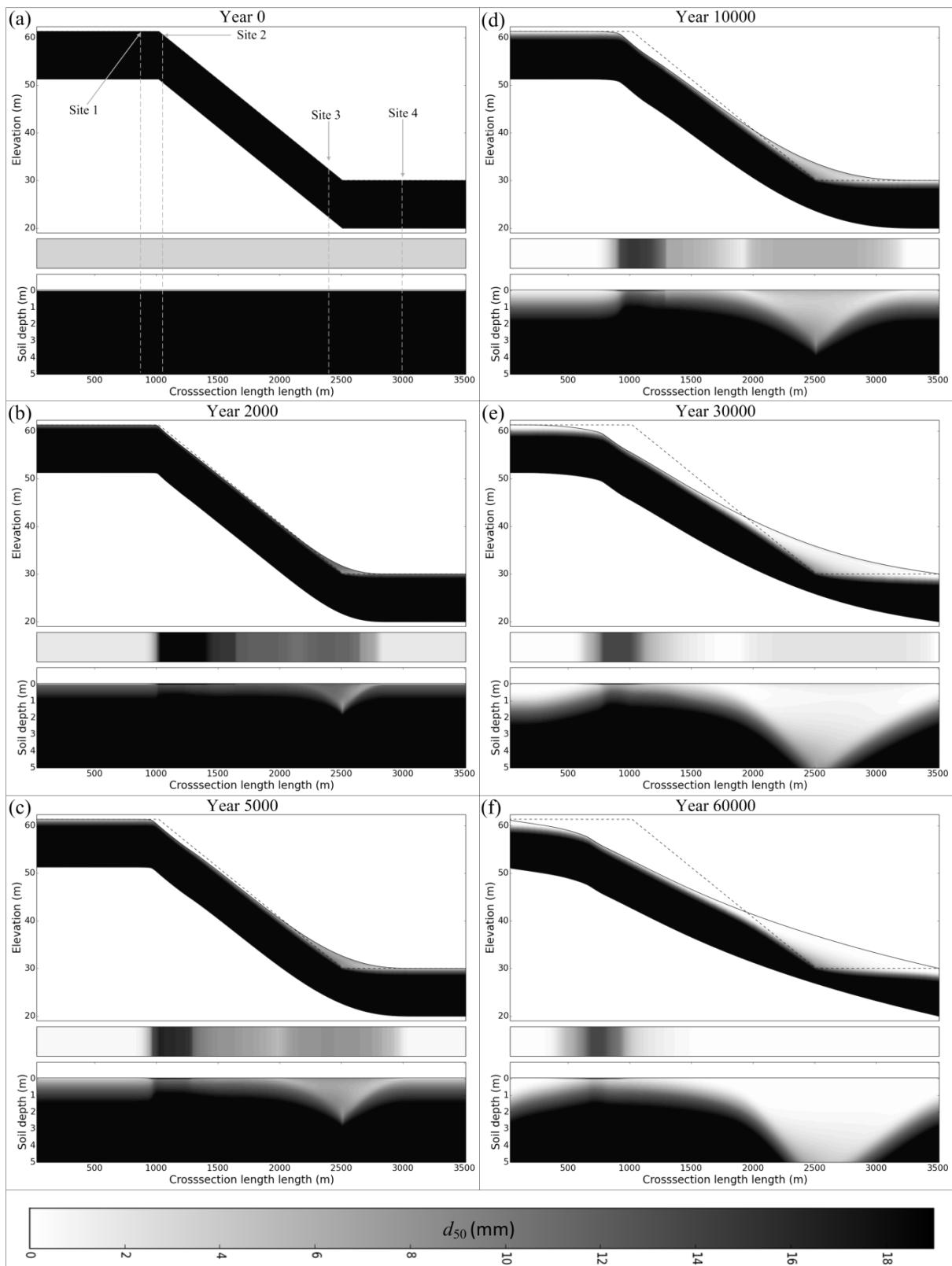
1010

1011

1012

Figure 6 Evolution of the soilscape with the exponential depth dependent weathering function.

Figure 6



1014

1015

1016

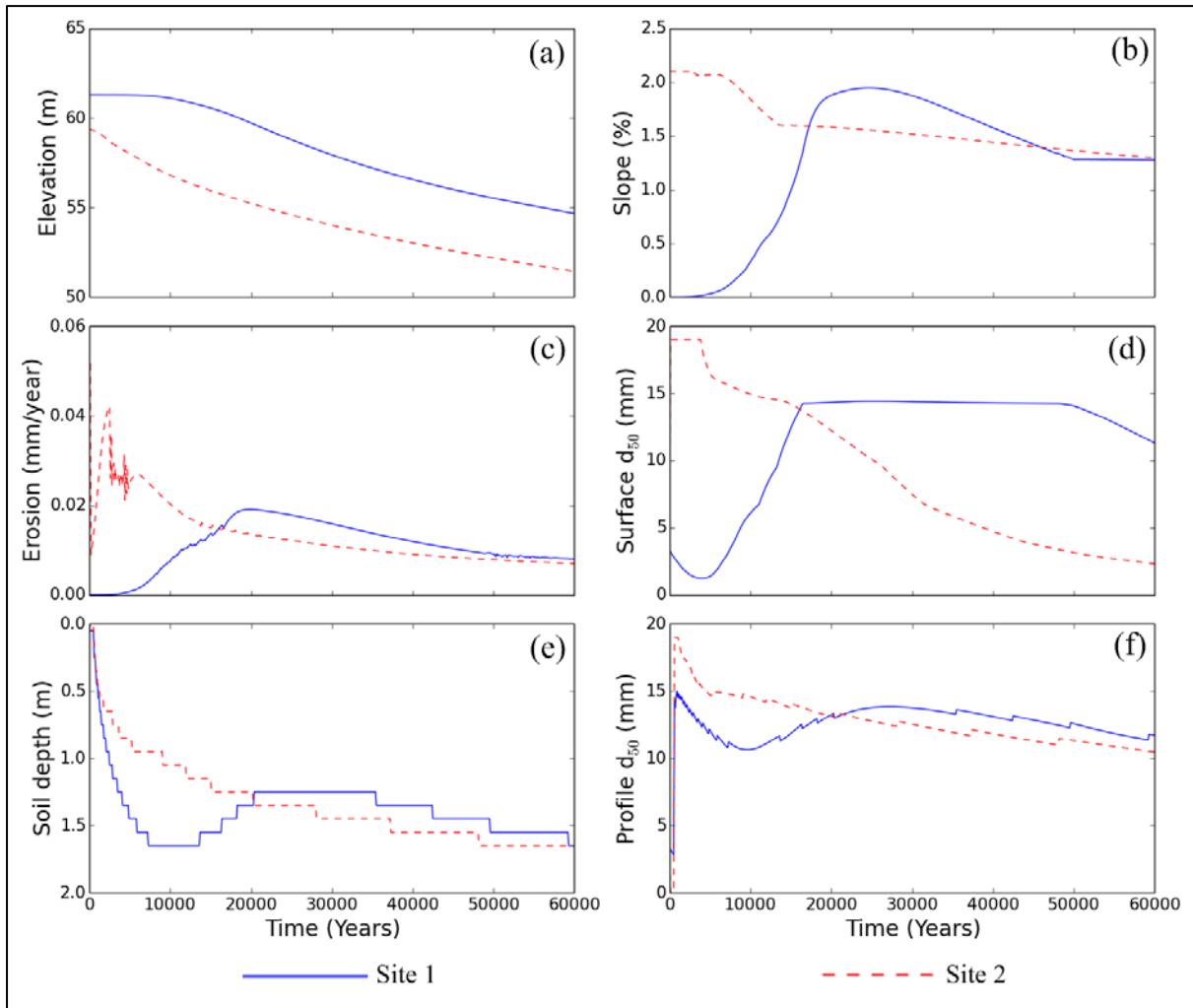
1017

Figure 6 Evolution of the soilscape with the exponential depth dependent weathering function.

1018

1019

Figure 7



1020

Figure 7 Evolution characteristics of Sites 1 and 2, (a) elevation, (b) hillslope gradient, (c) erosion rate, (d) surface d_{50} , (e) soil depth, and (f) profile d_{50} .

1023

1024

1025

1026

1027

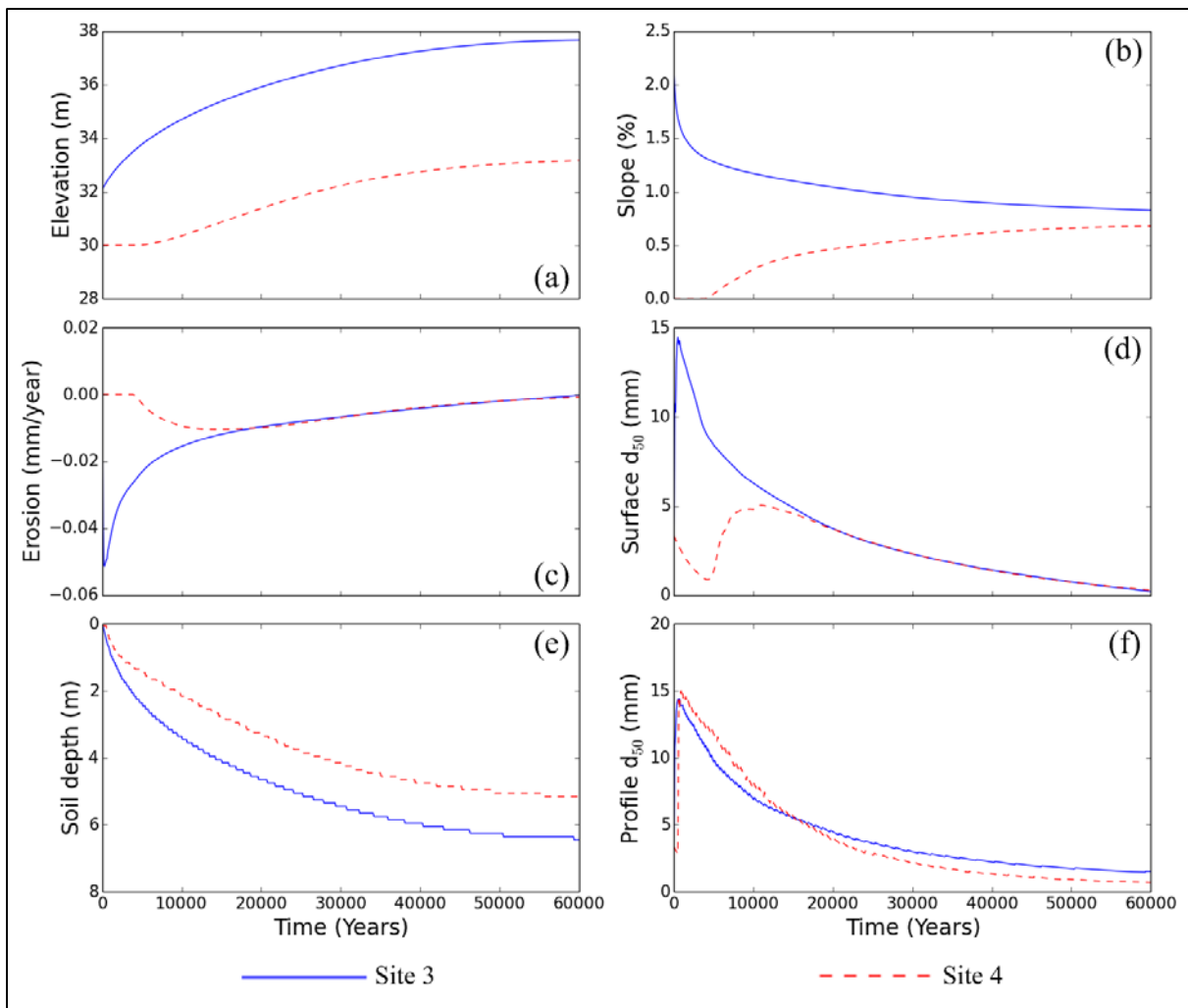
1028

1029

1030

1031

Figure 8



1032

1033 **Figure 8** Evolution (near the hillslope-valley boundary) of Sites 3 and 4, (a) elevation, (b)
1034 hillslope gradient, (c) erosion rate, (d) surface d_{50} , (e) soil depth, and (f) profile d_{50} .

1035

1036

1037

1038

1039

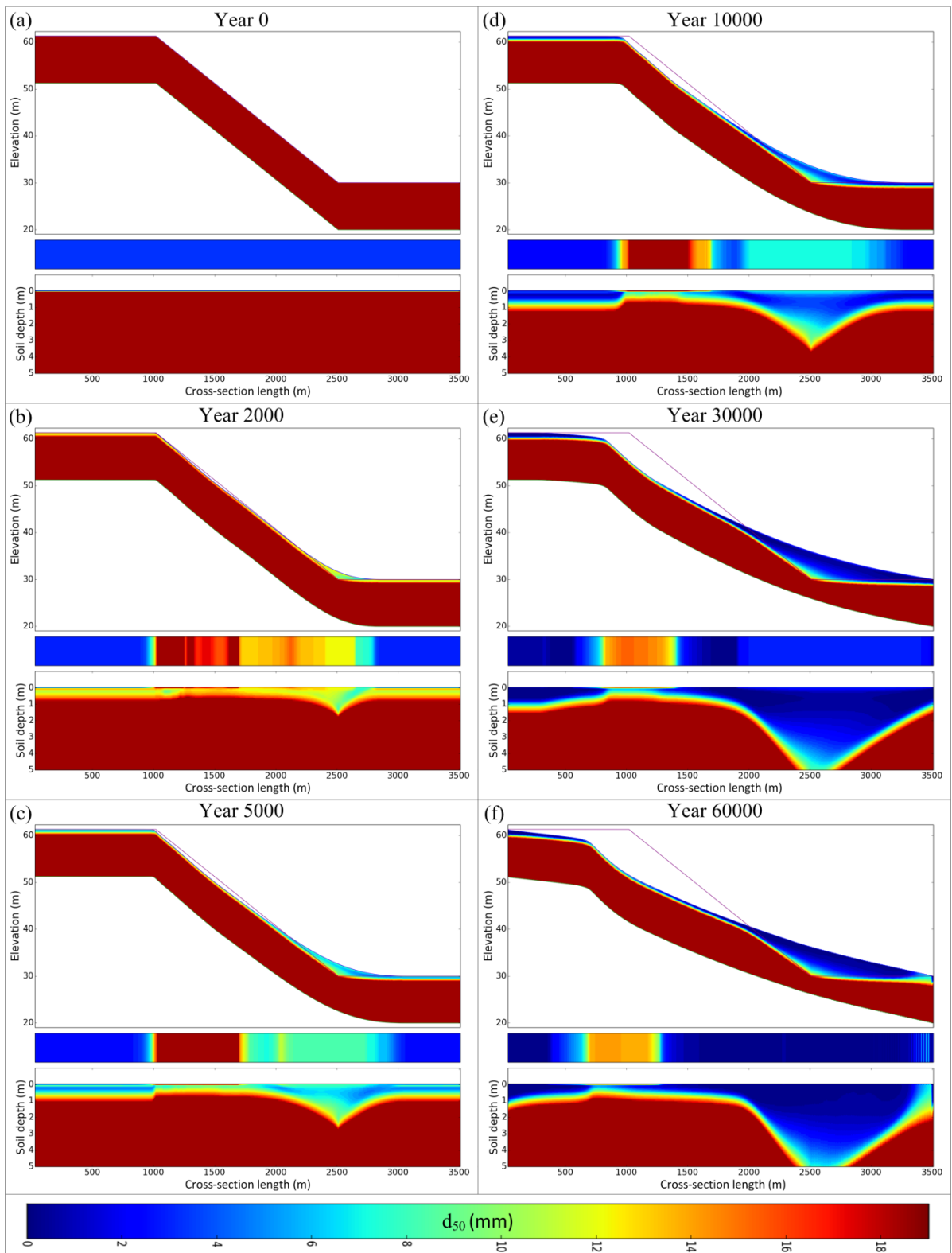
1040

1041

1042

1043

Figure 9



1045

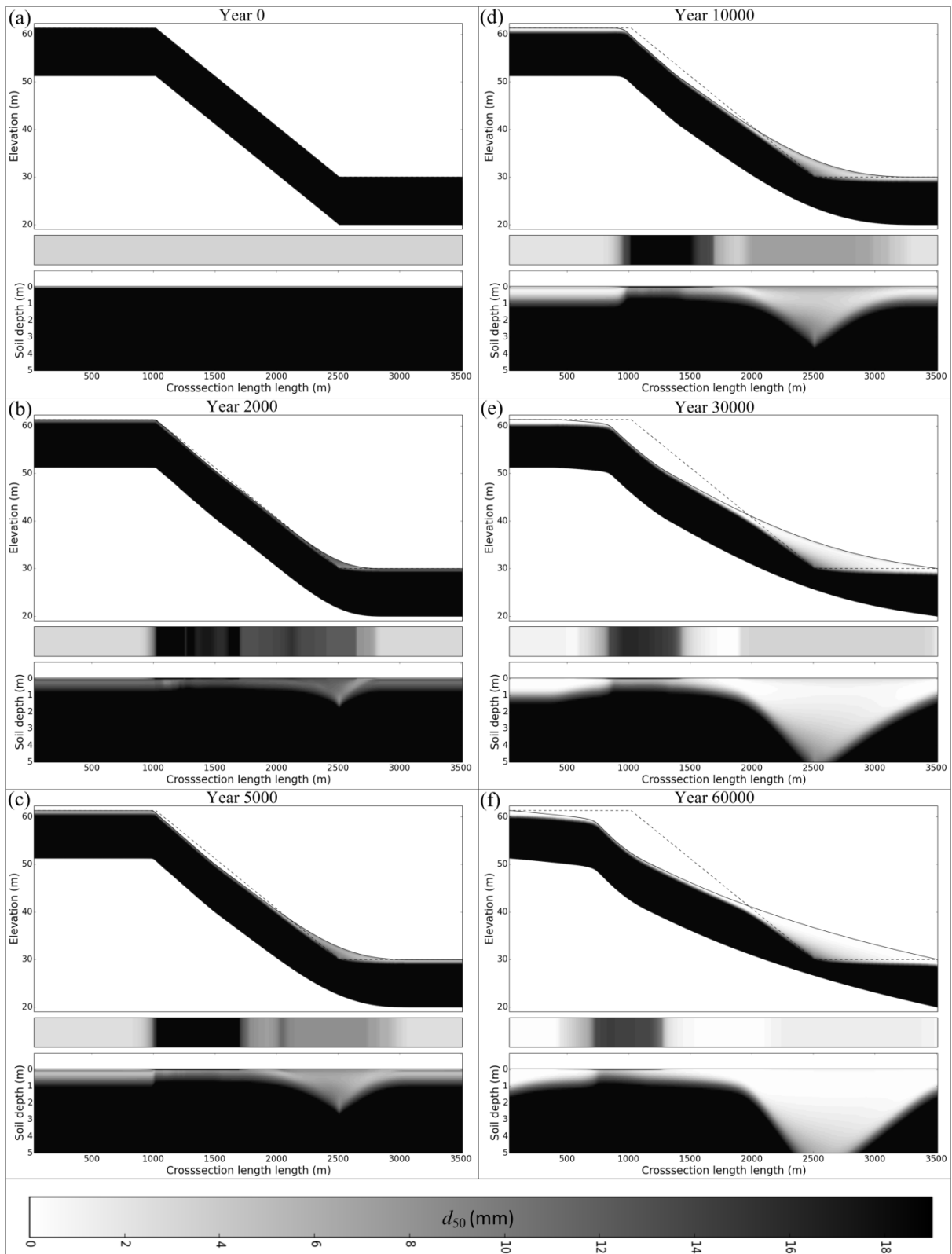
1046

1047

1048

Figure 9 Evolution of the soilscape with the humped exponential depth dependent weathering function.

Figure 9



1050

1051

1052

1053

Figure 9 Evolution of the soilscape with the humped exponential depth dependent weathering function.

1054

Table 1 Determination of erosion and deposition

Scenario	Condition	Actual erosion E_a ($kg\ s^{-1}$)	Deposition D ($kg\ s^{-1}$)
A	$L_{in} + E_p < T_c$	$T_c - L_{in}$	0
B	$L_{in} + E_p \geq T_c$	E_p	0
C	$L_{in} \geq T_c$	0	$L_{in} - T_c$

1055

1056

1057

1058

1059

1060

1061

1062

1063

1064

1065

1066

1067

1068

1069

1070

1071

1072

Table 2 Example calculation of adjustment vector \underline{K} .

<i>Size Class</i>	<i>Elements of $\underline{\psi}_{in}$ (ψ_z)</i>	<i>Entries of \underline{J} ($J_{z,z}$)</i>	<i>$J_{z,z} \psi_z$</i>	<i>Adjusted $J_{z,z} \psi_z$</i>	<i>Deficit / Surplus</i>	<i>Diagonal elements of \underline{K}</i>	<i>Entries of $\underline{\Phi}$</i>
<i>1</i>	<i>5.00</i>	<i>1.0</i>	<i>5.00</i>	<i>7.29</i>	<i>-2.29</i>	<i>-2.29</i>	<i>5.00</i>
<i>2</i>	<i>10.00</i>	<i>0.7</i>	<i>7.00</i>	<i>10.21</i>	<i>-0.21</i>	<i>-0.21</i>	<i>10.00</i>
<i>3</i>	<i>20.00</i>	<i>0.4</i>	<i>8.00</i>	<i>11.67</i>	<i>8.33</i>	<i>2.00</i>	<i>13.67</i>
<i>4</i>	<i>40.00</i>	<i>0.1</i>	<i>4.00</i>	<i>5.83</i>	<i>34.17</i>	<i>0.50</i>	<i>6.33</i>
<i>Total</i>	<i>75.00</i>		<i>24.00</i>	<i>35.00</i>			<i>35.00</i>

1073

1074

1075

1076

1077

1078

1079

1080

1081

1082

1083

1084

1085

1086

1087

Table 3 Soil grading distribution data used for SSSPAM simulation.

1088

1089

1090

Grading Range (mm)		Ranger1a	Ranger1b
0	- 0.063	1.40 %	0.0%
0.063	- 0.111	2.25 %	0.0%
0.111	- 0.125	0.75 %	0.0%
0.125	- 0.187	1.15 %	0.0%
0.187	- 0.25	1.15 %	0.0%
0.25	- 0.5	10.20 %	0.0%
0.5	- 1	9.60 %	0.0%
1	- 2	12.50 %	0.0%
2	- 4	16.40 %	0.0%
4	- 9.5	20.00 %	0.0%
9.5	- 19	24.60 %	100.0%